Finite element simulations of the Portevin-Le Chatelier effect in metal-matrix composites

Stéphanie Graff, Hanno Dierke, Samuel Forest, Hartmut Neuhäuser, Jean-Loup Strudel

Finite Element Simulations of the Portevin-Le Chatelier Effect in Metal-Matrix Composites

Journal:	*Philosophical Magazine & Philosophical Magazine Letters*
Manuscript ID:	TPHM-07-Dec-0386.R1
Journal Selection:	Philosophical Magazine
Date Submitted by the Author:	04-Mar-2008
Complete List of Authors:	Graff, Stephanie; Mines de Paris / CNRS / ParisTech, Centre des Matériaux UMR 7633 Dierke, Hanno; TU Braunschweig, Institut fur Physik der Kondensierten Materie Forest, Samuel; Mines de Paris / CNRS / ParisTech, Centre des Matériaux UMR 7633 Neuhauser, Hartmut; TU Braunschweig, Institut fur Physik der Kondensierten Materie Strudel, Jean-Loup; Mines de Paris / CNRS / ParisTech, Centre des Matériaux UMR 7633
Keywords:	ageing, computational mechanics
Keywords (user supplied):	Portevin Le Chatelier effect, metal matrix composite, finite element simulation

Philosophical Magazine,

Finite Element Simulations of the Portevin–Le Chatelier Effect in Metal–Matrix Composites

Stéphanie Graff[a], Hanno Dierke[b], Samuel Forest[a]*, Hartmut Neuhäuser[b], Jean–Loup Strudel[a],

[a] Mines Paris, ParisTech, CNRS UMR 7633
BP 87, 91003 Evry Cedex, France

[b] Institut für Physik der Kondensierten Materie,
TU Braunschweig, Mendelssohnstr. 3
38106 Braunschweig Germany

(revised)

Computational homogenization techniques are used to predict the mechanical behaviour of metal matrix composites made of Al_20_3 particles in a Al-3% Mg matrix exhibiting dynamic strain ageing. A simple strain ageing continuum model is identified to describe the Portevin–Le Chatelier effect observed in the bulk aluminium alloy. Periodic homogenization is shown to provide a correct description of the mechanical behaviour of the composite concerning the presence of serrations on the macroscopic stress–strain curve and the prediction of the critical strain. Finite Element simulations of random distributions of particles are also performed to confirm the prediction of the overall behaviour. Local plastic strain rate localization phenomena around the particles are analyzed for the periodic and random situations.

Keywords: Al-Mg metal–matrix composite, Finite Element, Portevin–Le Chatelier effect

1 Introduction

The Portevin–Le Chatelier (PLC) effect is often observed in Al-Mg alloys [1]. Microscopically, it results from the dynamic interaction of mobile dislocations and solute atoms. Mobile dislocations move by successive jerks between forest dislocations. Solute atoms then diffuse to and saturate dislocations while they are temporarily arrested at these obstacles [2]. Referred to as dynamic strain ageing (DSA), this mechanism can lead to negative strain rate sensitivity (SRS) in a range of applied strain rates $\dot{\varepsilon}$ where dislocations and solute atoms have comparable mobility [3]. If the applied strain rate falls into such an appropriate range and if sufficient interaction between dislocations (via their long–range stress fields) occurs [4], plastic flow becomes heterogeneous. Plastic strain and plastic strain rate are highly localized in narrow bands in the deformed specimen. Such bands are either stationary or propagative in a continuous or discontinuous manner. In the present work, these bands are called *plastic strain rate bands*. The observed PLC effect depends on testing conditions [5, 6, 7, 8, 9]: applied strain rate [10, 11] and temperature range [12]. Mg contents larger than 2–3% in Al-Mg alloys lead to a pronounced PLC effect according to [13]. Field measurements techniques have clearly revealed the nature of such plastic strain rate bands. They range from early video–camera recording [1] to thermography [14, 15] and image correlation analyses [16, 7].

The Al-Mg alloys are used in a large variety of industrial applications owing to their high mechanical strength and low density. Their practical benefit is limited by PLC instabilities and strain heterogeneities. The study of Estrin and Lebyodkin [17] and the experimental work of Dierke [18, 19] have shown the influence of the addition of dispersed second phase Al_2O_3 particles to the parent Al-3% Mg alloy on the unstable deformation and the critical conditions for the occurrence of PLC instabilities.

The present work is motivated by recent progress in the simulation of PLC effects in specimens and components. It is possible to reproduce the types of PLC bands observed in experiments as well as their

*Corresponding author. Email: samuel.forest@ensmp.fr

Philosophical Magazine
ISSN 1478-6435 print/ISSN 1478-6443 online © 200x Taylor & Francis
http://www.tandf.co.uk/journals
DOI: xxxxxxxx

dynamic behavior using finite element (FE) simulations. The basic assumption is the DSA mechanism which is introduced in the model of Kubin–Estrin *et al.* in a phenomenological way [20]. Theoretical predictions of instabilities for negative strain rate sensitivity are possible based on this class of models [21]. Zhang *et al.* [22] propose a 3–dimensional macroscopic constitutive model including the time dependence of the solute concentration at temporarily arrested dislocations. Their FE simulations show the occurrence of propagative zones of localized strain for an Al-Mg-Si alloy in flat and round specimens associated with serrations on the macroscopic stress–strain curve during tensile tests at constant strain rate. Beaudoin *et al.* [23] develop a polycrystalline plasticity constitutive model embedded in a FE framework. Their simulations reproduce both the propagative and stochastic nature of PLC bands. The model of Schmauder and Hähner [24] introduces an activation enthalpy for dislocation motion which is considered as an intrinsic variable governing the extent to which dislocations are saturated by solute clouds. However this model and the model of Zhang *et al.* provide similar results in the presented simulations. Graff *et al.* [25, 26] use the macroscopic model of [22] to account for both dynamic and static strain ageing. Their FE analyses show that complex strain localization phenomena take place at notches and crack tips in several strain ageing materials. They suggest that these localization phenomena can play a significant role in early fracture processes. The numerical analyses of integration time–step and mesh dependence performed in [27, 28] show that finite element simulations of these unstable phenomena provide numerically reliable predictions of critical strain, amplitude of serration and band orientation within the context of elastoviscoplasticity.

In the present work, the experimental results on Al-3% Mg alloys reinforced with Al_2O_3 dispersion particles obtained by [18] are simulated by FE computations using the model of Graff *et al.* [25, 26] and based on the theory of composites [29]. The question is raised whether conventional homogenization techniques like periodic homogenization can be used in the presence of elastoviscoplastic instabilities of the PLC type. Finite Element simulations of PLC effects have not been performed in the context of heterogeneous materials yet, especially for composites. The objective of this work is to show numerical predictions of the impact of the initiation and scattering of PLC bands at particles on the effective properties of the composite. The results are compared to the experimental observations of [18, 19].

The conventional macroscopic properties such as the critical strain for serrations and the types of serrations observed on the stress–strain curve are analysed for various applied strain rates and volume fractions of particles. The mesh size sensitivity and the influence of particles distribution, periodic vs. random, are discussed. The predicted strain rate localization processes close to particles are analyzed.

Section 2 recalls the identification of the material parameters of the model in the case of the bulk parent Al-3% Mg alloy, called AA5754, as performed in [18]. This model is then used in section 3 to predict the behavior of the composite material based on periodic homogenization methods. The simulation results are compared with the corresponding experimental tests. The discussion of section 4 addresses the sensitivity to mesh size in the FE model and the influence of randomness of particle distribution on the behavior of the composite.

2 Simulations for the parent Al-3% Mg alloy

2.1 *Salient experimental features*

The PLC effects are classified according to the type of serrations observed on the macroscopic stress–strain curves, usually labeled types A, B and C [1]. For an Al-3% Mg alloy at room temperature, type A, B and C bands are associated with applied strain rates ranging from $\dot{\varepsilon} = 10^{-3}s^{-1}$, $\dot{\varepsilon} = 10^{-4}s^{-1}$, to $\dot{\varepsilon} = 10^{-5}s^{-1}$ respectively [30]. Type A appears as a continuous propagation of PLC bands which are usually nucleated near one grip of the specimen. The bands propagate with nearly constant velocity and band width to the other end of the specimen. Type B bands propagate discontinuously along the specimen. More precisely, small strain bands nucleate in the nearest surroundings of the former band. Type C deformation is characterized by spatially random bursts of bands without significant propagation accompanied by large and high frequency load drops.

For an Al-3% Mg alloy, the dependence of the critical strain ε_c corresponding to the onset of serrations, on the applied strain rate exhibits various types of behavior: (i) "normal" behaviour for which ε_c increases

with $\dot{\varepsilon}$, (ii) "inverse" behaviour for which ε_c decreases with $\dot{\varepsilon}$ and (iii) "inverse then normal" [13].

Experiments were performed on flat specimens with a gauge part of 54 mm × 4 mm × 1.5 mm in size prepared from polycrystalline cold–rolled sheets of Al-3% Mg alloy. The first material studied in this work was the bulk parent Al-3% Mg alloy. All specimens were heat treated for recovery after rolling (5h at 673K) and quenched in water. The average grain size obtained after heat treatments is estimated at about 70 μm. The uniaxial tensile tests were performed at constant cross–head speed using a screw–driven tensile machine Instron 1185 at room temperature. The range of strain rates applied was $1.1\text{x}10^{-5}$ to $6.3\text{x}10^{-3}$ s^{-1}. Further details on material testing and characterization can be found in [18, 19].

The tests have also been performed on metal matrix composites (abbreviated MMC) made of the matrix aluminium alloy 5754 and Al_20_3 particles (diameter 3 μm). The considered volume fractions of particles are 2 and 5%.

2.2 *Constitutive equations and identification of the strain ageing model*

The macroscopic model presented in [22] is available to simulate instabilities in materials containing interstitial or substitutional elements that can segregate to dislocations and alter their mobility. It incorporates in a set of phenomenological constitutive equations several features of the intrinsic behavior of strain ageing materials and can be used to simulate both the PLC effect and the Lüders behaviour as shown in [25, 26]. The evolution equations mimic the mechanisms of repeated breakaway of mobile dislocations temporarily arrested at forest obstacles and by solute atmospheres. The model is formulated here within the small strain framework. It has been checked in [28] that the introduction of large strain effects, at least in the strain range investigated in this work, does not affect the type and amplitude of serrations and localization bands.

The total deformation is the sum of elastic and plastic strain tensors:

$$\underset{\sim}{\boldsymbol{\varepsilon}} = \underset{\sim}{\boldsymbol{\varepsilon}}^e + \underset{\sim}{\boldsymbol{\varepsilon}}^p, \quad \underset{\sim}{\boldsymbol{\sigma}} = \underset{\sim}{\boldsymbol{C}} : \underset{\sim}{\boldsymbol{\varepsilon}}^e \tag{1}$$

The tensor $\underset{\sim}{\boldsymbol{C}}$ is the fourth–rank tensor of elastic moduli and $\underset{\sim}{\boldsymbol{\sigma}}$ is the stress tensor. The yield criterion is defined by:

$$f(\underset{\sim}{\boldsymbol{\sigma}}) = J_2(\underset{\sim}{\boldsymbol{\sigma}}) - R, \quad J_2(\underset{\sim}{\boldsymbol{\sigma}}) = \sqrt{\frac{3}{2}\underset{\sim}{\boldsymbol{s}} : \underset{\sim}{\boldsymbol{s}}} \tag{2}$$

J_2 is the second invariant of the stress tensor and $\underset{\sim}{\boldsymbol{s}}$ is the deviatoric part of the stress. The plastic flow rule is deduced from the normality law:

$$\underset{\sim}{\dot{\boldsymbol{\varepsilon}}}^p = \dot{p}\,\frac{\partial f}{\partial \underset{\sim}{\boldsymbol{\sigma}}} = \frac{3}{2}\dot{p}\frac{\underset{\sim}{\boldsymbol{s}}}{J_2(\underset{\sim}{\boldsymbol{\sigma}})}, \quad \dot{p} = \dot{\varepsilon}_0 \exp\left(\frac{< f(\underset{\sim}{\boldsymbol{\sigma}}) >}{K}\right) \tag{3}$$

$\dot{p}$ is the cumulative plastic strain rate (in s^{-1}). The brackets $< f(\underset{\sim}{\boldsymbol{\sigma}}) >$ mean the maximum of $(f(\underset{\sim}{\boldsymbol{\sigma}}), 0)$. Material parameters $\dot{\varepsilon}_0$, K are introduced and depend on temperature. At each instant, the yield stress R is given by

$$R = R_0 + Q(1 - \exp(-bp)) + P_1 C_s, \quad \text{with} \quad C_s = C_m(1 - \exp(-P_2 p^{\alpha} t_a^n)) \tag{4}$$

where $R_0 + Q(1 - \exp(-bp))$ is the isotropic strain hardening. The isotropic strain ageing term $P_1 C_s$ corresponds to the stress associated with DSA. It depends on the local plastic strain rate through the time t_a, called the ageing time. The variable C_s is an estimation of the over–concentration of solute atoms segregating around the dislocation lines which are temporarily immobilized by extrinsic obstacles. It takes the maximal value C_m corresponding to the saturated concentration around the dislocations. These constitutive equations involve the material parameters R_0, Q, b, P_1, P_2, α and n. In fact, only the product $P_1 C_m$ can be identified from the tensile curves, so that we take $C_m = 1$ by convention. An exponent n

equal to 1/3 instead of the Cottrell–Bilby exponent 2/3 is adopted and attributed to "pipe diffusion" of solute atoms along dislocation lines [31]. Along the macroscopic curve, the switch between low and high C_s during the segregation process is achieved through the "relaxation–saturation" kinetics of Avrami for t_a according to McCormick [32]:

$$\dot{t}_a = \frac{t_w - t_a}{t_w}, \quad \text{with} \quad t_w = \frac{\omega}{\dot{p}} \tag{5}$$

where t_w is the waiting time experienced by dislocations between successive strain bursts of amplitude ω when the applied strain rate is $\dot{p}$. This simple approximation of the model in [4] is used here for easier handling in the computer code. To reduce the number of material parameters, the parameter ω was treated as a constant in this work. It is, in general, a function of cumulative plastic strain p.

The simplifications of the model therefore include:
(i) McCormick's relation instead of Hähner's waiting time distributions;
(ii) Elementary strain is assumed to be constant instead of the variation with a maximum [33] or linear increase ([34] for Cu-Mn, [12] for Al-Mg). The effect will be small and not relevant for qualitative results;
(iii) The model does not account for the inverse PLC effect, as it will be seen in the following.

The previous model was implemented in the FE program Z–set [35]. The differential equations are integrated at each Gauss point of each element using a Runge–Kutta method of fourth order with automatic time–stepping. The resolution method for global balance is based on an implicit Newton algorithm. Quadratic elements with reduced integration are used in all the simulations of this work, except in section 4.2 where linear elements are used. Plane stress conditions are enforced in the 2D FE simulations. 2D finite element simulations under plane stress conditions are known to favour strain localization phenomena because the out of plane strain compatibility is not ensured: the first localization band may occur earlier than in 3D and the stress drops may be more pronounced [36]. However, these differences generally are not sufficient to invalidate the 2D prediction. The 2D simulations still provide a correct prediction of overall curves and types of bands in the case of PLC effect as checked in [37].

This model has been shown in references [22, 25, 27] to be able to account for several macroscopic features of PLC effects. However, precise identifications of material parameters with respect to tensile curves at different strain rates remain seldom in the literature. Most simulations are based on closely related values of parameters for which the instabilities are observed. In reference [18] such a precise identification was undertaken to accurately reproduce the negative strain rate sensitivity domain for the considered aluminium alloy at room temperature. The identification of the model must be done at two levels: (i) volume elements, corresponding to assumed homogeneous deformation, can be considered for fixing hardening parameters, viscosity parameters $K, \dot{\varepsilon}_0$, and also the S–shape of the stress/strain rate curve, (ii) structural computations involving non–homogeneous deformation are necessary to determine essentially the parameter ω strongly related to the plastic strain carried by the PLC bands. A systematic procedure for the identification of the material parameters of the strain–ageing model is presented in [28].

For the purpose of identification, 2–dimensional FE analyses were carried out for straight specimens. The mesh of the plate is shown in figure 1(a). Figure 1(a) also shows the boundary conditions for the straight plate specimen geometry. The total length was equal to 12.5 mm and the width was 2.5 mm. The vertical displacement at the bottom was fixed to zero. The vertical displacement at the top was prescribed at a constant displacement rate. An initial defect was introduced in a single element into the specimen (lower yield stress) in order to trigger the first plastic strain rate band. The position and the value of this defect do not affect significantly the simulation results. The strain in the $\sigma(\varepsilon)$ curves always means global strain, i.e. strain is referred to the gauge length. In the simulations, we use the entire length of the plate to compute the overall strain. The ratio of length/width in the simulations was 5 compared to 13.5 in the experiment.

The identification of the material parameters describing the initiation and propagation of the plastic strain rate bands was performed on uniaxial tensile tests at the strain rates mentioned above at room temperature. The resulting material parameters are listed in table 1 for the parent Al-3% Mg alloy. The initial condition for the ageing time t_a required by the differential equation (5) was $t_a(0) = 0$.

2.3 *Simulation results*

The objective of this subsection is to show that the strain ageing model with the set of parameters of table 1 is able to reproduce the typical PLC curves and the various types of serrations depending on the applied strain rate. Three constant strain rates are selected for the simulations of the uniaxial tensile tests using straight specimens: 6.2 $10^{-3}s^{-1}$, 1.1 $10^{-4}s^{-1}$ and 1.1 $10^{-5}s^{-1}$.

Figure 2 compares the overall calculated macroscopic stress–strain curves obtained for the various applied strain rates. Several types of PLC serrations can be observed depending on the strain rates. Some characteristics of PLC effects in an Al-3% Mg alloy mentioned in section 2.1 are reproduced in these calculated tensile curves. The slight negative strain rate sensitivity and the type of serrations can be seen. Comparison between simulation and experiment is shown in figure 3. In figures 2 and 3, but also in figure 5, the simulations curves are stopped at different times because at that points the time steps became too small due to the strong instabilities.

At $\dot{\varepsilon} = 6.2\ 10^{-3}s^{-1}$, the macroscopic curve exhibits type A serrations. Each macro–step on the stress-strain curve corresponds to the reflection of one plastic strain rate band at one end of the specimen. Such a plastic strain rate localization band is shown in the finite element mesh of the plate on the left of the top curve in figure 3.

At $\dot{\varepsilon} = 1.1\ 10^{-4}s^{-1}$, type B serrations are observed. The propagation of the plastic strain rate bands is not continuous. Intermittent propagation of a single band is observed. The contour of plastic strain rate in the mesh at the left of the middle curve of figure 3 reveals two clearly formed bands and two disappearing bands.

Then, at $\dot{\varepsilon} = 1.1\ 10^{-5}s^{-1}$, mixed type A+B serrations are characterized by well defined successive irregular serrations followed by strong stress increases. Only hopping bands propagating over a small number of elements are observed during the tensile test, as shown in the mesh on the left of the bottom curve. Note that the identified value of $\dot{\varepsilon}_0$ is 2.5 larger than the lowest strain rate in the tensile tests considered in this work. Since an exponential function is used in the model for the viscoplastic flow rule according to equation (3), instead of a sinh function, the consequence is that the deformation of the simulated tensile test on a plate cannot be homogeneous and necessarily takes place in the form of PLC bands in which the strain rate is larger than the overall strain rate. We have also performed the three tensile tests with the value $\dot{\varepsilon}_0 = 1 \times 10^{-5}$ s^{-1} without significant change of the tensile curves.

The bands propagate at an angle of about 53° with respect to the tensile axis, for purely mechanical reasons. A detailed description of the band formation and propagation can be found in [24].

The critical strain ε_c marks the onset of serrations in the tensile curves. In the experimental curves, a serration can be detected as soon as its amplitude is significantly higher than the measurement intrinsic fluctuations. In the simulations, two criteria could be adopted that lead to values of the critical strains that were in good agreement, at least in the case of an homogeneous plate in tension: first serration on the overall curve on the one hand, and first plastic strain rate localization band where $\dot{p}$ is at least twice higher than the overall strain rate. The critical strain is found to be a monotonic function of the applied strain rate. The obtained values are given in table 2 and compared to the experimental results. A very good accordance is found for the two highest strain rates. However, the model is not able to reproduce the higher critical strain for the lowest strain rate. In particular, even with a value $\dot{\varepsilon}_0 = 1 \times 10^{-5}$ s^{-1}, the critical strain obtained for the tensile test at $\dot{\varepsilon} = 1.1 \times 10^{-5}$ s^{-1} is still too small compared to the experimental results. More elaborate constitutive equations could be taken from the literature to account for this non monotonic evolution of the critical strain. It has not been undertaken in this work.

Table 2 also gives the value of the plastic strain rate inside the propagating bands in the computed plate in tension. It is about 20 times higher than the prescribed overall strain rate, except at the lowest strain rate for which the ratio is even larger. It depends on the width of the band and therefore is, in general, mesh–dependent.

As a conclusion, the identified strain ageing model is a good candidate for simulating the influence of particles in AA5754 MMC, even though the “inverse” behavior of the critical strain is not yet accounted for.

3 Application to the AA5754 MMC

The AA5754 MMC is made of the matrix material studied in the previous section containing a dispersion of Al_2O_3 particles with a given volume fraction f. The objective of this section is to see whether the effective behavior of the MMC can be predicted from the knowledge of the constitutive law of the matrix and assuming unshearable and unbreakable elastic particles, based on classical computational homogenization methods for composites. Two main difficulties arise when applying the mechanics of composites to the case of the AA5754 MMC. First, the validity and prediction capability of homogenization methods for composites are ensured only when the behaviour of the constituents is stable. In the presence of local instabilities like strain localization, the existence of a representative volume element is not even ensured and an effective behavior may not exist in all cases. This is especially the case in the damage of composites [38]. The second difficulty is due to the relatively small size of the particles, of about 3 μm size, for which classical continuum mechanics may fail at predicting the real hardening effect.

3.1 *Periodic homogenization method*

Standard homogenization procedures used for composite materials [29] are applied now to the AA5754 MMC. Periodic homogenization is the most straightforward approach to handle particle composites. It usually provides a correct approximation of the overall behavior at least for small volume fractions of particles, even though the actual materials are not periodic [39]. A 2–dimensional unit cell corresponding to an hexagonal distribution of circular inclusions is adopted. This situation is rather well–suited for fiber composites with parallel fibers along the third direction. Under plane stress or generalized plane strain conditions, such 2D simulations usually provide correct estimations of the behaviour of particle composites, as shown in [40, 41]. Plane stress (resp. generalized plane strain) models generally underestimate (resp. overestimate) the overall elastoplastic properties of the MMC. Such comparisons between 2D and 3D models for MMC can be found in [42, 43]. In the presence of severe instabilities expected in the simulation of strain ageing effects in heterogeneous materials and leading to a high computational cost, the first step consists in performing 2D computations, as proposed in this work. The following computations have been performed on a single 1.2GHz PC (1Go RAM) under Linux.

Figure 1(b) shows a 1–inclusion unit cell for a particle volume fraction $f = 2\%$. It is based on a periodic assumption with a honeycomb particle distribution that results in isotropic in–plane elastic properties and quasi–isotropic elastoplastic in plane behaviour. Plane stress conditions are enforced in the simulations. The impact of the choice of one unit cell and the influence of randomness are investigated in section 4.

The constitutive model of the parent Al-Mg alloy identified in the previous section is used to describe the behavior of the matrix (see table 1). The Al_2O_3 particles are regarded as elastic with a Young's modulus equal to 370000 MPa and a Poisson ratio equal to 0.22.

Periodic boundary conditions are applied to the unit cell. The displacement vector u_i at each node of the mesh takes the form:

$$u_i = E_{ij} x_j + v_i \tag{6}$$

The node coordinates are x_i. The components E_{ij} denote the mean applied strain. The fluctuation v_i is periodic, meaning that it takes the same value at homologous points on opposite sides of the unit cell. The nodal forces are anti–periodic at homologous points on opposite sides of the unit cell. A classical result of periodic homogenization is that the mean strain over the unit cell V is:

$$E_{ij} = \frac{1}{V} \int_V \varepsilon_{ij}^{local} \, dv = \frac{1}{V} \int_V \frac{1}{2} (u_{i,j} + u_{j,i}) \, dv \tag{7}$$

The resulting stress is computed as the mean value of the local stresses over the unit cell. The components E_{ij} are additional degrees of freedom in the FE program. The associated reaction forces are the components of the mean stress. As a result, it is possible to impose mixed loading conditions, i.e. a prescribed axial

mean strain E_{22} and vanishing remaining components of the mean stress tensor. These periodic overall tensile conditions are used in the next section. The mean tensile strain E_{22} is simply called ε in the following and the mean axial stress is called σ.

The simulation of the development of PLC bands in the matrix requires extremely small time steps to reach a correct description of their local propagation and of the overall serrations on the macroscopic curve. As a result, computation times of one to six days were necessary to obtain the results presented in this work, especially for the fine meshes considered in section 4.2.

Simulations of the MMC behaviour were carried out for various overall applied strain rates and volume fractions of particles.

3.2 *Simulation results and comparison with the parent Al-3% Mg alloy*

The first objective of this part is to describe the effect of particles on the simulated macroscopic stress–strain curves, in particular the type of serrations and the critical strain for serrations ε_c. These results are compared with the simulations of the parent Al-3% Mg alloy. The main findings are summarized in table 3.

Figure 4 gives the computed stress–strain curves at $\dot{\varepsilon} = 6.2\ 10^{-3} s^{-1}$ for various volume fractions of particles. They are compared with the simulation results of the parent Al-3% Mg alloy. Classically, in the theory of composites, the addition of Al_2O_3 particles in the matrix leads to a strengthening of the macroscopic behavior.

The addition of particles modifies the type of serrations. Serrations are observed on the mean stress–strain curves but their amplitude and frequency are smaller for the MMC than for the bulk alloy. The values of the critical strain for serrations ε_c are smaller for MMCs than for the parent Al-3% Mg alloy for the same overall applied strain rate as shown in table 3. The critical strain ε_c is found to increase when the volume fraction f of particles increases.

The apparent yield stress on the overall curves of figure 4 turns out to be almost independent of the volume fraction. It is close to the yield stress of the matrix. In contrast, the work hardening of the composite is higher than that of the bulk material. It is found to increase with increasing volume fraction (see figure 4).

The effect of the applied strain rate on the computed stress–strain curve for $f = 2\%$ is shown in figure 5. A negative SRS is observed for the composite. This effect is also shown in figure 2 for the parent Al-3% Mg alloy but it is more pronounced in the MMC. Figure 5 also shows that the work–hardening of the MMC increases with decreasing strain rate. The type of serrations observed on the overall stress–strain curves of the composite is the same for the three tested strain rates, in strong contrast to the case of the parent alloy (see figure 2) for which type A and B types of serrations could clearly be distinguished. The amplitude of serrations is found to decrease when the volume fraction increases.

The second objective of this part is to study the plastic strain rate fields inside the unit cell. These observations provide the explanation for several of the macroscopic effects described previously. The presence of the inclusion induces stress concentrations around the particle. As a result, the first strain rate localization bands starts in the close neighbourhood of the inclusion. The fields of plastic strain rate inside the unit cell are given in figure 6 for different overall strain levels. Several parallel bands are seen to originate at the inclusion and to propagate further inside the matrix. In contrast to the simulation of homogeneous plates in tension where single bands could be observed, several bands are always obtained simultaneously in the case of MMC simulations. Irrespective of strain rate and volume fraction, the computed composite responses exhibit the same qualitative behaviour in terms of band propagation and serrations. This is probably due to the intrinsically heterogeneous stress–strain field around the inclusion. It is not possible at this stage to determine the type of macroscopic PLC bands from the simulations since we obtain multi–site band initiation and propagation which results, according to the periodic hypothesis, in simultaneous activation of bands in the entire sample.

The formation of the first plastic strain rate band is found to coincide with the first serration on the macroscopic curve, i.e. for $\varepsilon = \varepsilon_c$. This explains why the critical strain for serrations is slightly smaller for the MMC than in the bulk alloy. Two competing effects are responsible for the dependence of ε_c with

respect to volume fraction f. On the one hand, the stress concentration effect leads to smaller values of ε_c. On the other hand, for a given mean strain rate $\dot{\varepsilon}$, higher volume fractions of particles in the composite lead to higher mean strain rates in the matrix since the deforming volume is reduced. Table 3 shows that the plastic strain rate localized in the bands is three times larger for the MMC with $f = 2\%$, five times larger for the MMC with $f = 5\%$ and six times larger for the MMC with $f = 10\%$ than for the parent Al-3%Mg alloy. This effect will postpone the occurrence of strain rate bands in the matrix. As a result of both effects, the values of ε_c for the bulk alloy and for the MMC with $f = 10\%$ turn out to be very close.

The stress concentration effect is responsible for the fact that the initial yield stress is almost unaffected by the volume fraction of particles. The increase in work hardening rate with decreasing applied strain rate is due to DSA: lower strain rates with longer waiting times at obstacles lead to an increase in the breakaway stress of dislocations.

3.3 *Experiment vs. simulation results for MMC*

Experiments were performed on flat specimens with a gauge length of 54 mm × 4 mm × 1.5 mm in size prepared from polycrystalline cold–rolled sheets of Al-3% Mg alloy and reinforced with Al_2O_3 particles. The average diameter of particles was about 3 μm. All specimens were heat treated for recovery after rolling (5h at 673K) and water quenched. Three different volume fractions of particles were tested: $f = 2\%$, $f = 5\%$ and $f = 10\%$. The uniaxial tensile tests were performed at constant strain rate at room temperature.

The experimental study shows that the addition of dispersed particles to the Al-3% Mg alloy affects the type of serrations as compared with the matrix material [18]. This effect is shown in figure 7 for $f = 2\%$ and $f = 5\%$ at $\dot{\varepsilon} = 6.2\ 10^{-3}s^{-1}$. Serrations do not disappear in the composite behaviour but they are significantly reduced. The simulation results reproduce correctly the type of serrations and the decrease in amplitude of the stress drops. The type of serrations does not depend on the strain rate nor volume fraction, contrary to the case of the bulk alloy (see figures 4 and 5). This is also a feature correctly predicted by the simulation.

It can be noted that the strengthening effect of the particles predicted by the homogenization model is not observed experimentally. Experimental curves for the MMC even lie slightly below the response of the parent alloy. A discussion of this experimental feature is given in the reference [18]. It is mainly attributed there to stress concentrations already existing in the composite before testing as a result of specimen preparation (heat treatments) and to possible damage of the composite.

The general trend observed in the experimental results is a reduction of the critical strain ε_c in the MMC as compared to the matrix. A remarkable agreement is obtained between simulation and experiment regarding the prediction of the critical strain, as shown in table 3, except for $f = 10\%$. The values of the critical strain for serrations are close for samples with $f = 2\%$ and $f = 5\%$. This observation is also made in [17] for an Al-3% Mg alloy reinforced with Al_2O_3 particles at $\dot{\varepsilon} = 2.10^{-5}s^{-1}$ at room temperature. These authors show also that ε_c is the lowest for specimens with $f = 10\%$. They correlate this effect with the clustering of particles. Indeed an increase in the volume fraction of particles favors clustering. The specimens with a small volume fraction of particles exhibit a more homogeneous distribution of particles. As a consequence, larger volumes free of particles exist inside a specimen with high volume fraction of particles so that the mechanical behavior of the specimen on the whole is determined by the matrix material to a higher degree. It is consistent with the hypothesis that the particles mainly limit the mean free path of the plastic bands.

4 Discussion

The simple composite model has been shown to provide a correct description of several features of the experimental MMC behaviour compared to that of the parent alloy. However, several aspects must be discussed to confirm these predictions. They mainly deal with the assessment of the accuracy of the numerical simulations, on the one hand, and with the impact of the assumption of periodicity in the previous model, on the other hand.

4.1 *Mesh sensitivity and impact of periodicity constraint*

In the simulation of strain localization phenomena, the analysis of the mesh size sensitivity of the results is an important issue. For that purpose, two mesh sizes of the considered unit cell were considered: (i) 1–inclusion unit cell with one mesh size of figure 1(b), (ii) 1–inclusion unit cell with a twice finer mesh size. The macroscopic curves of figure 6(a) result from the simulations of tensile tests at $\dot{\varepsilon} = 6.2\ 10^{-3} s^{-1}$ using either mesh sizes. They show that:

(i) The tensile curves are almost identical. In particular, the critical strains for serrations are equal ($\varepsilon_c = 0.014$).
(ii) The width of the plastic strain rate bands is always equal to about one element. Consequently the band width is mesh dependent. However it does not affect the mean response. This is also confirmed by systematic numerical analysis in [27, 28].
(iii) The orientation of the band with respect to the tensile axis is mesh–independent (it is about 53°).

In the presence of strain localization phenomena, the spacial periodicity of the particle distribution is not necessarily reflected in the strain field. That is why we investigate also the influence of the content of the simulated unit cell on the predicted response of the MMC. Two different unit cells are investigated: (i) a 1–inclusion unit cell (see figure 1(b)), (ii) a 9–inclusion unit cell (see figure 8(a)). Periodic conditions are applied to the outer boundaries in both cases. The results of the simulations clearly indicate that the number of cells has almost no influence on the macroscopic curves as shown in figure 6(a). However PLC serrations are slightly less pronounced using the 9–inclusion unit cell than for the 1–inclusion unit cell. The simulated plastic strain rate patterns inside the 9–inclusion unit cell are shown at four different strain levels in figure 9. They can be compared to the plastic strain rate fields in the 1–inclusion unit cell of figure 6. The overall strain levels for which the fields are observed are indicated on the macroscopic curves of figure 6(a). The regions with high plastic strain rates are always located directly close to particles, where local stress concentrations develop, in the first step of figures 6 and 9, in 1–inclusion unit cell and 9–inclusion unit cell respectively. For $\varepsilon = 0.017$, the plastic strain rate fields around particles are almost identical for the 1–inclusion and 9–inclusion unit cells. After a mean strain of about 0.019, the strain rate band patterns differ significantly for 1 and for 9 inclusions. The number of bands inside the central inclusion of the 9-inclusion cell is smaller than in the 1-inclusion unit cell. This corresponds to a periodicity breaking of the strain localization patterns. This shows that, even in the presence of multiple sites for initiation of instabilities, plastic strain rate tends to localize in a small number of bands. This suggests that strain localization bands may be observed at the macroscopic scale instead of the multi–site localization patterns over the whole sample associated with the 1–inclusion unit cell model. This is a strong limitation of the application of periodic homogenization in the presence of local instabilities. This effect however has no influence on the type of serrations and the critical strain for serrations, as shown in figure 6(a), at least for the small number of inclusions considered here.

4.2 *Impact of a random distribution of particles*

The actual geometrical distribution of particles in real materials is not periodic. The influence of a random distribution of particles of one single size on the simulation of PLC effects is investigated in this subsection. Images containing identical circular particles were generated following a Poisson distribution. The mesh of the corresponding unit cells was made of linear triangular elements. A regular mesh could be used for the plate and periodic unit cells including quadratic elements with reduced integration as recommended in plasticity in the presence of localization bands. In the case of random distribution of particles, only a free meshing technique could be applied. Since the bands cross the entire specimen, the same element size must be used in the whole sample. This procedure results in a large number of small triangular elements. Due to the large number of elements, it was not possible to use quadratic triangular elements. Computations on a regularly meshed plate and a plate with free linear triangles, for a same number of degrees of freedom, have been performed to check that the overall serrations and the types of bands are very close.

Two volume fractions of particles are considered: $f = 2\%$ and $f = 5\%$. The meshes are shown in figure 8 (b), (c) respectively.

Two mechanical tests were performed: A tensile test at $\dot{\varepsilon}_{22} = 6.2\ 10^{-3}s^{-1}$ and a shear test at $\dot{\varepsilon}_{12} = 6.2\ 10^{-3}s^{-1}$. The simulation of shear tests makes it possible to obtain different orientations of the PLC bands and to compare the resulting equivalent stress/equivalent strain curves to the case of tension. These curves are expected to be close, as a result of the isotropic behaviour of the matrix and in plane isotropic distribution of particles.

For the tensile test, a vertical displacement is applied at the top of the mesh and the lateral surfaces are free of forces. Homogeneous strain conditions are applied at the boundary for the shear tests: The displacement at the boundary is then given by equation (6) with $v_i = 0$.

The macroscopic stress–strain curves for the tensile tests are plotted for both volume fractions in figure 10. It has been checked that the equivalent von Mises stress–strain curves obtained for the shear tests are almost identical to the tensile curve. This confirms the isotropic character of the distribution of particles even for the single image of the microstructure considered here. The plastic strain rate maps for the tensile test are shown in figure 11 and for the shear test in the figures 12 and 13 for $f = 2\%$ and $f = 5\%$ respectively, and at different overall strain levels indicated on the macroscopic curve of figure 6.

The overall stress levels are found to be very close for a random distribution and for a periodic one. However, in contrast to the periodic case, the tensile curves obtained with a random distribution of particles exhibit almost no serration, although the same small time steps were used in both simulations to capture possible serrations. Simulations with larger numbers of inclusions and various types of boundary conditions would be necessary to confirm this point. The scenario for the initiation and the propagation of plastic strain rate bands is similar in both random and periodic cases. In the case of tension, the PLC bands are bent in the vicinity of particles and deviate from the usual 54° orientation. In the shear tests, horizontal and vertical PLC bands are observed (see figures 12 and 13), which are in agreement with the prediction of classical strain localization criteria [36]. In tension and shear, several bands are always observed simultaneously at different locations showing the multi–site character of the plastic strain rate localization phenomena. The random distribution seems to promote multiple activation of PLC bands in contrast to the 9–inclusion cell model investigated previously.

The simulations with a random distribution of particles suggest that it may be possible to reduce or even suppress overall serrations in the effective behaviour of strain ageing metals by incorporating particles that act as initiation and scattering sites for strain rate localization bands. The experimental results do not completely confirm this expectation. This point is important from the industrial point of view and is discussed in the reference [18]. Such a scattering effect is illustrated by figure 14. A single vertical band, indicated by an arrow, propagates through the matrix and hits a particle. Two short horizontal bands form at the poles of the inclusion when the band goes through the obstacle. The vertical band recovers its initial shape once the obstacle has been overcome.

The structure of plastic deformation in figure 11 to 14 exhibits a clear patterning of strain rate localization bands with a more of less regular spacing, especially in shear, related to the spacing of particles. On the one hand, the particles do not disturb significantly the propagation of long localization bands that extend over the whole width of the microstructure window. On the other hand, the particle spacing seems to dictate an overall regular patterning of the bands. A thorough statistical analysis is required to conclude on this question of patterning of localization bands which is out of the scope of this work. In particular, the effect of boundary conditions (periodic, mixed and strain based, as used in this work) on the structure of plastic deformation field in the random material must be studied in a systematic way.

5 Conclusions and prospects

The strain ageing model implemented in a FE code was used to predict the influence of a dispersion of Al_2O_3 particles in a parent Al-3% Mg alloy, based on classical computational homogenization techniques for composites. The main features of the PLC effect in the bulk alloy and the influence of particles can be summarized as follows:

(i) The strain ageing model is able to quantitatively account for the negative SRS in the parent Al-3% Mg alloy. The simple strain ageing model could be identified to satisfactorily describe several features of the

experimental behaviour of this alloy. Type A serrations, type B (intermittent propagation) and types A+B (with very fine serrations followed by sudden larger load jumps) observed on the macroscopic stress–strain curves are reproduced in a quantitatively accurate manner.

(ii) The simulations results for MMCs show that introducing a dispersion of particles in the material leads to a decrease of the amplitude of PLC serrations on the macroscopic curve and a reduction of the critical strain for serrations. The critical strain ε_c is found to increase with increasing volume fraction f. Two competing mechanisms were evidenced in the simulations, namely the stress concentration effect close to the particles and the effect of higher local strain rates induced by the presence of particles. The same type of serrations was found for the three investigated strain rates.

(iii) The simulation results for a periodic distribution of particles and for a random distribution of particles give similar and reliable predictions of the overall stress–strain curves for MMC including PLC effects. The random distribution of particles leads to a significantly lower amplitude of serrations on the macroscopic curve. However plastic strain rate localization bands still develop and propagate but on a finer spacial scale than for the bulk material.

(iv) Although the macroscopic curve is identical for both 1–inclusion and 9–inclusion unit cells, the simulation results predict differences in the plastic strain rate band patterns that finally break the spatial periodicity.

(v) Complex multiple–site strain rate localization phenomena are obtained when the random character of the microstructure is taken into account. They explain the reduction of load drops on the macroscopic curves and can give indications for the design of more stable strain ageing MMCs. They deserve a future systematic computational analysis in relation to random distribution of sizes, spacing and clustering of particles and size of the considered volume element.

The conventional computational homogenization methods turn out to provide reliable results for composites in the presence of local viscoplastic instabilities. This is due to a specific feature of DSA constitutive modeling, namely the fact that the domain of negative strain rate sensitivity remains bounded in a finite strain rate range. The positive strain rate sensitivity that always exists at sufficiently high strain rates acts as a stabilizing factor promoting band propagation and band spreading instead of further localization. Material instability remains therefore only a transient feature of the local material response. This can ensure the existence of an effective material response, in contrast to strain softening of damaging materials. This explains also the quasi–mesh–independence of the overall curves obtained in this work, even though individual localization bands always are one–element thick.

Complex strain localization phenomena take place in strain ageing MMC even if PLC serrations are reduced on the macroscopic curve. Accordingly, neglecting them in the design of engineering components is not without consequences regarding the prediction of fracture processes. The relations between dynamic strain ageing and fracture mechanisms, revealed by many available experimental results, are currently the subject of extensive field measurement analyses in [44] for shear banding, and of computational investigations on the loss of ductility in necking and ductile fracture [45, 46].

Acknowledgements

The authors thank F. N'Guyen for providing pictures with the random distribution of particles and K. Madi for meshing these pictures. The authors wish to acknowledge the financial support provided through the European Community's Human Potential Programme under contract HPRN-CT-2002-00198, (DEFINO project), and the DFG (Deutsche Forschungsgemeinschaft).

References

[1] K. Chihab, Y. Estrin, L.P. Kubin, and J. Vergnol. The kinetics of the Portevin–Le Chatelier bands in an Al–5%Mg alloy. *Scripta Metallurgica*, 21:203–208, 1987.

[2] A. Van den Beukel. Theory of the effect of dynamic strain aging on mechanical properties. *Physica Status Solidi*, 30:197–206, 1975.
[3] Y. Estrin and L.P. Kubin. *Continuum Models for Materials with Microstructure, H. Mühlhaus, editor*, chapter Spatial coupling and propagative plastic instabilities, pages 395–450. Wiley, 1995.
[4] M. Zaiser and P. Hähner. Oscillatory modes of plastic deformation: theoretical concepts. *Physica Status Solidi B*, 199:267–330, 1997.
[5] A. Ziegenbein, P. Hähner, and H. Neuhäuser. Propagating Portevin–Le Chatelier deformation bands in Cu–15at.%Al polycrystals: experimental and theoretical description. *Materials Science and Engineering A*, 309–310:336–339, 2001.
[6] R. Shabadi, S. Kumar, H.J. Roven, and E.S. Dwarakadasa. Effect of specimen condition, orientation and alloy composition on PLC band parameters. *Materials Science and Engineering A*, 382:203–208, 2004.
[7] Q. Zhang, Z. Jiang, H. Jiang, Z. Chen, and X. Wu. On the propagation and pulsation of Portevin–Le Chatelier deformation bands: an experimental study with digital speckle pattern metrology. *International Journal of Plasticity*, 21:2150–2173, 2005.
[8] H. Jiang, Q. Zhang, X. Chen, Z. Chen, Z. Jiang, X. Wu, and J. Fan. Three types of Portevin–Le Chatelier effects: Experiment and modelling. *Acta Materialia*, 55:2219–2228, 2007.
[9] N. Ranc and D. Wagner. Experimental study by pyrometry of Portevin–Le Chatelier plastic instabilities–Type A to type B transition. *Materials Science and Engineering A, in press*, 2007.
[10] F.B. Klose, A. Ziegenbein, J. Weidenmüller, H. Neuhäuser, and P. Hähner. Portevin–Le Chatelier effect in strain and stress controlled tensile tests. *Computational Materials Science*, 26:80–86, 2003.
[11] P. Hähner, A. Ziegenbein, E. Rizzi, and H. Neuhäuser. Spatiotemporal analysis of Portevin–Le Chatelier deformation bands : theory, simulation and experiment. *Physical review*, B65:134109–1–134109–20, 2002.
[12] C.P. Ling and P.G. McCormick. The effect of temperature on strain rate sensitivity in an Al–Mg–Si alloy. *Acta metallurgica et materialia*, 41(11):3127–3131, 1993.
[13] K. Chihab, H. Ait-Amokhtar, and K. Bouabdellah. Serrated yielding due to Portevin–Le Chatelier effect in commercial Al–Mg alloys. *Ann. Chim. Sci. Mat.*, 27:69–75, 2002.
[14] H. Louche, P. Vacher, and R. Arrieux. Thermal observations associated with the Portevin–Le Chatelier effect in an Al–Mg alloy. *Materials Science and Engineering A*, 404:188–196, 2005.
[15] N. Ranc and D. Wagner. Some aspects of Portevin–Le Chatelier plastic instabilities investigated by infrared pyrometry. *Materials Science and Engineering A*, 394:87–95, 2005.
[16] W. Tong, H. Tao, N. Zhang, and L.G. Hector. Time–resolved strain mapping measurements of individual Portevin–Le Chatelier deformation bands. *Scripta materialia*, 53:87–92, 2005.
[17] Y. Estrin and M.A. Lebyodkin. The influence of dispersion particles on the Portevin–le Chatelier effect: from average particle characteristics to particle arrangement. *Materials Science and Engineering A*, 387–389:195–198, 2004.
[18] H. Dierke, F. Krawehl, S. Graff, S. Forest, J. Šachl, and H. Neuhäuser. Portevin–Le Chatelier effect in AlMg alloys: Influence of obstacles, experiments and modelling. *Computational Materials Science*, 39:106–112, 2007.
[19] F. Chmelík, F.B. Klose, H. Dierke, J. Šachl, H. Neuhäuser, and P. Lukáč. Investigating the Portevin–Le Chatelier effect in strain rate and stress rate controlled tests by the acoustic emission and laser extensometry techniques. *Materials Science and Engineering A*, 462:53–60, 2007.
[20] L.P. Kubin, Y. Estrin, and C. Perrier. On static strain ageing. *Acta metallurgica et materialia*, 40(5):1037–1044, 1992.
[21] A. Benallal, T. Borvik, A. Clausen, and O. Hopperstad. Dynamic strain aging, negative strain-

rate sensitivity and related instabilities. *Technische Mechanik*, 23:160–166, 2003.

[22] S. Zhang, P.G. McCormick, and Y. Estrin. The morphology of Portevin–Le Chatelier bands : finite element simulation for Al–Mg–Si. *Acta Materialia*, 49:1087–1094, 2001.

[23] S. Kok, M.S. Bharathi, A.J. Beaudoin, C. Fressengeas, G. Ananthakrishna, L.P. Kubin, and M. Lebyodkin. Spatial coupling in jerky flow using polycristal plasticity. *Acta Materialia*, 51:3651–3662, 2003.

[24] G. Lasko, P. Hähner, and S. Schmauder. Finite element simulation of the Portevin–Le Chatelier effect. *Modelling Simul. Mater. Sci. Eng.*, 13:645–656, 2005.

[25] S. Graff, S. Forest, J.-L. Strudel, C. Prioul, P. Pilvin, and J.-L. Béchade. Strain localization phenomena associated with static and dynamic strain ageing in notched specimens: experiments and finite element simulations. *Materials Science and Engineering A*, 387–389:181–185, 2004.

[26] S. Graff, S. Forest, J.-L. Strudel, C. Prioul, P. Pilvin, and J.-L. Béchade. Finite element simulations of dynamic strain ageing effects at V–notches and crack tips. *Scripta Materialia*, 52:1181–1186, 2005.

[27] A. Benallal, T. Berstad, T. Borvik, A.H. Clausen, and 0.S. Hopperstad. Dynamic strain aging and related instabilities: experimental, theoretical and numerical aspects. *European Journal of Mechanics A/solids*, 25:397–424, 2006.

[28] M. Mazière, J. Besson, S. Forest, B. Tanguy, H. Chalons, and F. Vogel. Numerical modelling of the Portevin–Le Chatelier effect. *European Journal of Computational Mechanics, in press*, 2008.

[29] E. Sanchez-Palencia and A. Zaoui. *Homogenization techniques for composite media*. Lecture Notes in Physics No. 272, Springer, Berlin, 1987.

[30] M. Lebyodkin, Y. Bréchet, Y. Estrin, and L. Kubin. Statistical behaviour and strain localization patterns in the Portevin–Le Chatelier effect. *Acta Materialia*, 44:4531–4541, 1996.

[31] J. Friedel. *Dislocations*. Pergamon, 1964.

[32] Y. Estrin and P.G. McCormick. Modelling the transient flow behaviour of dynamic strain ageing materials. *Acta metallurgica et materialia*, 39:2977–2983, 1991.

[33] L.P. Kubin and Y. Estrin. Evolution of dislocation densities and the critical conditions for the portevin-le chatelier effect. *Acta metallurgica et materialia*, 38:697–707, 1990.

[34] A.W. Springer and C. Schwink. Quantitative inverstagations on dynamic strain ageing in polycrystalline cumn alloys. *Scripta Metallurgica*, 25:2739–2744, 1991.

[35] Z–set package. www.nwnumerics.com, www.mat.ensmp.fr. 2001.

[36] J. Besson. *Local approach to fracture*. Ecole des Mines de Paris–Les Presses, 2004.

[37] M. Mazière. *Burst of turboengine disks*. Phd, Ecole des Mines de Paris, 2007.

[38] I.M. Gitman, H. Asked, and L.J. Sluys. Representative volume: Existence and size determination. *Engineering Fracture Mechanics*, 74:2518–2534, 2007.

[39] N. Ohno, X. Wu, and T. Matsuda. Homogenized properties of elastic–viscoplastic composites with periodic internal structures. *International Journal of Mechanical Sciences*, 42:1519–1536, 2000.

[40] A. Borbély, H. H. Biermann, and O. O. Hartmann. FE investigation of the effect of particle distribution on the uniaxial stresss–train behaviour of particulate reinforced metal-matrix composites. *Materials Science and Engineering*, A313:34–45, 2001.

[41] E. Soppa, S. Schmauder, G. Fischer, J. Brollo, and U. Weber. Deformation and damage in Al/Al_2O_3. *Computational Materials Science*, 28:574–586, 2003.

[42] H.J. Böhm and W. Han. Comparisons between three-dimensional and two-dimensional multiparticle unit cell models for particle reinforced metal matrix composites. *Modelling Simul. Mater. Sci. Eng.*, 9:47–65, 2001.

[43] D. Saraev and S. Schmauder. Finite element modelling of Al/SiCp metal matrix composites with particles aligned in stripes: a 2D/3D comparison. *International Journal of Plasticity*,

19:733–747, 2003.

[44] H. Halim, D.S. Wilkinson, and M. Niewczas. The Portevin–Le Chatelier (PLC) effect and shear band formation in an AA5754 alloy. *Acta materialia*, 55:4151–4160, 2007.

[45] O.S. Hopperstad, T. Borvik, T. Berstad, O.G. Lademo, and A. Benallal. A numerical study on the influence of the Portevin–Le Chatelier effect on necking in an aluminium alloy. *Modelling and Simulation in Materials Science and Engineering*, 15:747–772, 2007.

[46] J. Belotteau, C. Berdin, S. Forest, A. Parrot, and C. Prioul. From static to dynamic strain aging: Modeling the mechanical behavior of a ferritic steel over the (20-350)°C temperature range. *International Journal of Plasticity, submitted*, 2008.

Table 1. Parameters of the strain ageing model for the parent Al-3% Mg alloy at room temperature.

Parameters	Units	Al-3% Mg alloy
R_0	MPa	73
Q	MPa	165
b	-	16
P_1	MPa	34
C_{m}	-	1
P_2	s^{-n}	3.91
n	-	0.33
α	-	0.44
ω	-	10^{-4}
$\dot{\varepsilon}_0$	s^{-1}	2.5×10^{-5}
K	(MPa)	0.615

Table 2. Critical conditions for the occurrence of PLC instabilities in the simulation results according to different applied strain rates for the parent Al-3% Mg alloy.

Influence of the applied strain rate $\dot{\varepsilon}$ (s^{-1})	Critical strain for onset of serrations ε_c (-) simulations / experiments	Plastic strain rate localized in the band (s^{-1})	Type of serrations
$6.2\ 10^{-3}$	0.018 / 0.017	0.03	A
$1.1\ 10^{-4}$	0.006 / 0.007	0.0018	B
$1.1\ 10^{-5}$	0.005 / 0.051	0.0018	A+B

Table 3. Critical strain for serrations in the simulation results at $\dot{\varepsilon} = 6.2\ 10^{-3} s^{-1}$ according to the volume fraction of particles for the AA5754 MMC and comparison with the parent Al-3%Mg alloy.

Influence of the volume fraction of particles f	Critical strain of serrations ε_c (-) simulations / experiments	Plastic strain rate localized in the band (s^{-1})	Type of serrations
Al-3%Mg alloy	0.018 / 0.017	0.03	A
$f = 2\%$	0.014 / 0.015	0.09	indeterminate
$f = 5\%$	0.015 / 0.015	0.14	indeterminate
$f = 10\%$	0.017 / 0.008	0.19	indeterminate

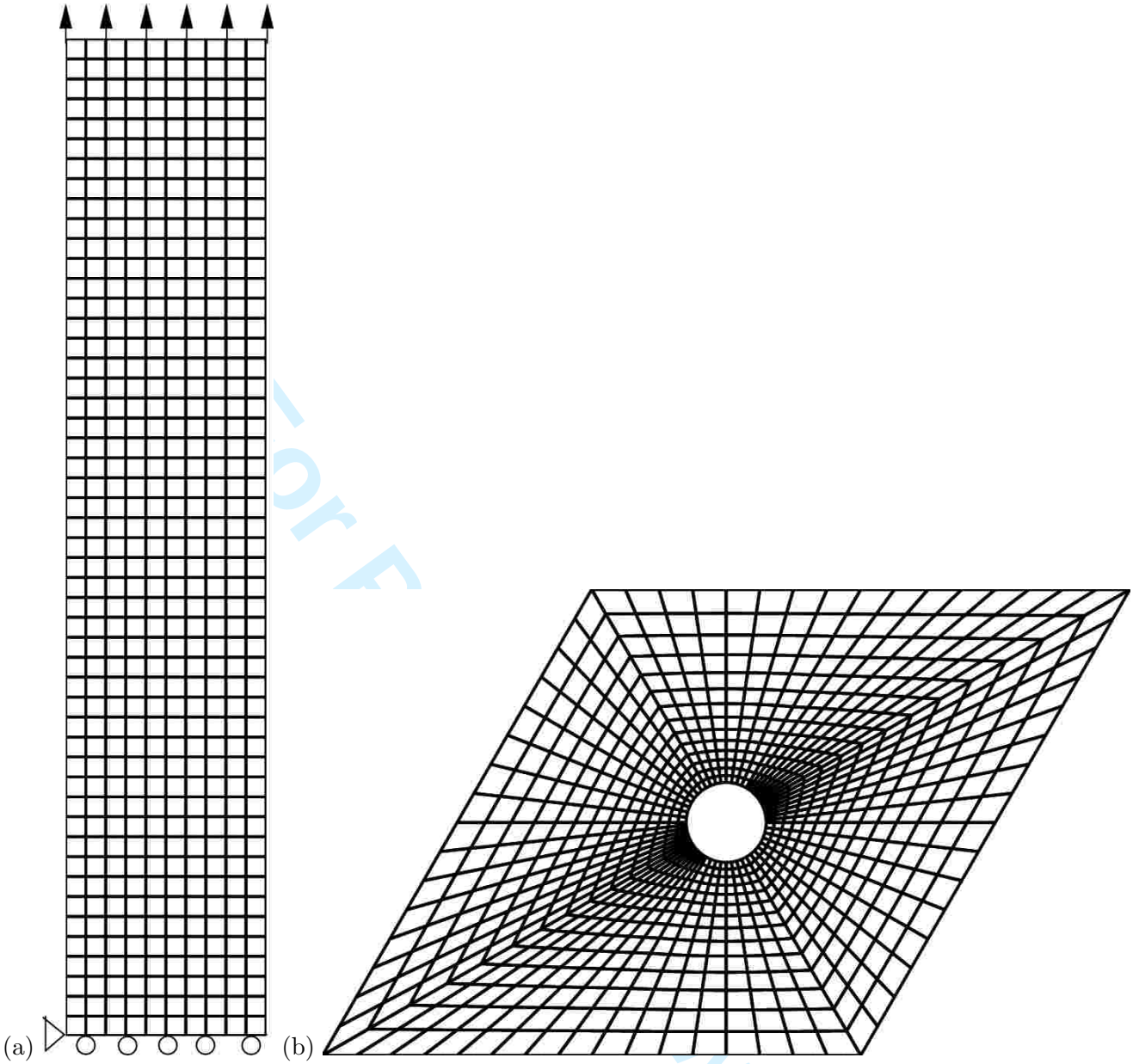

Figure 1. Finite element mesh for two specimen geometries: (a) straight plate specimen, (b) 1–inclusion unit cell for periodic homogenization with $f = 2\%$.

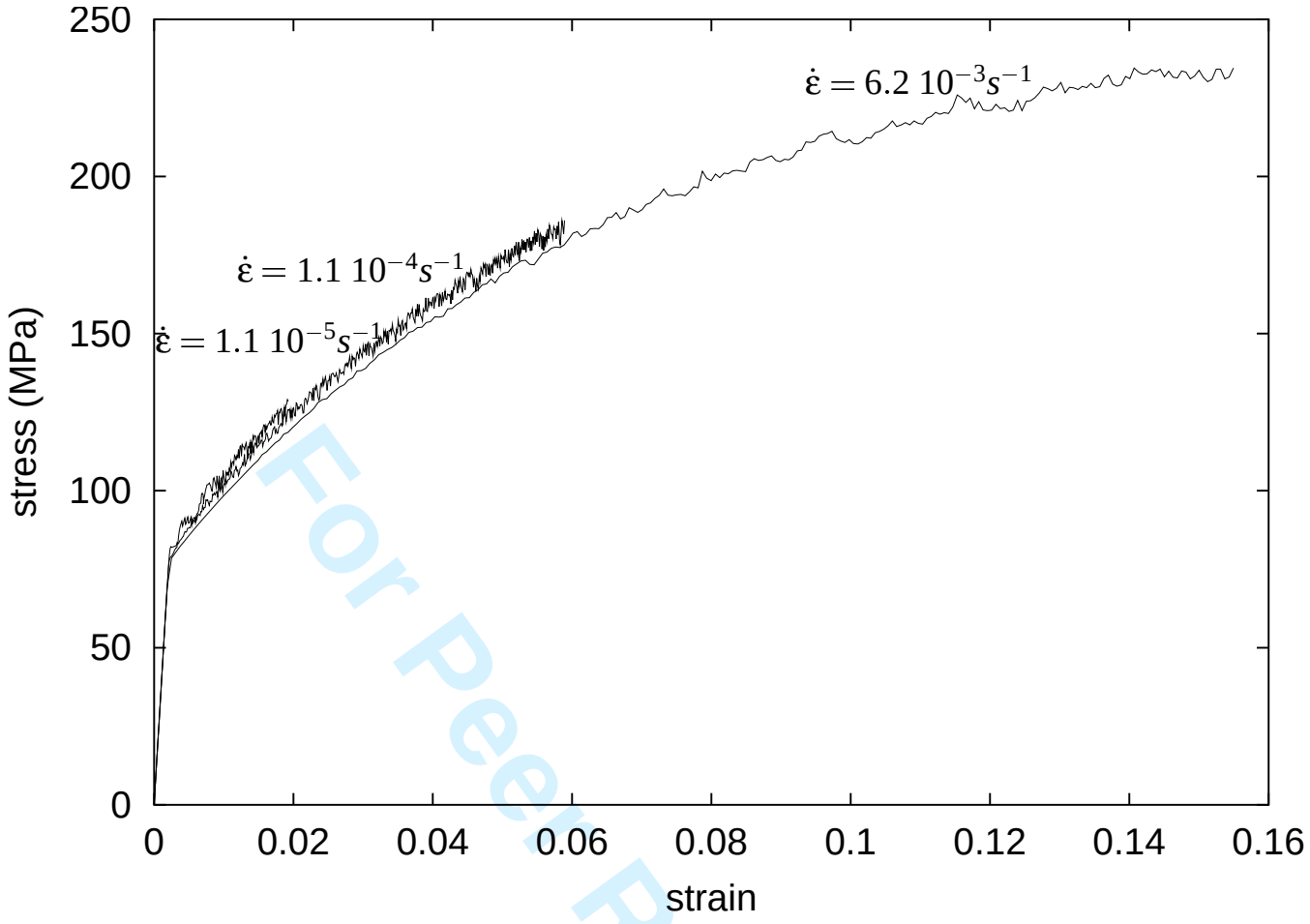

Figure 2. Influence of the applied strain rate on the computed stress–strain curves for the parent Al-3% Mg alloy.

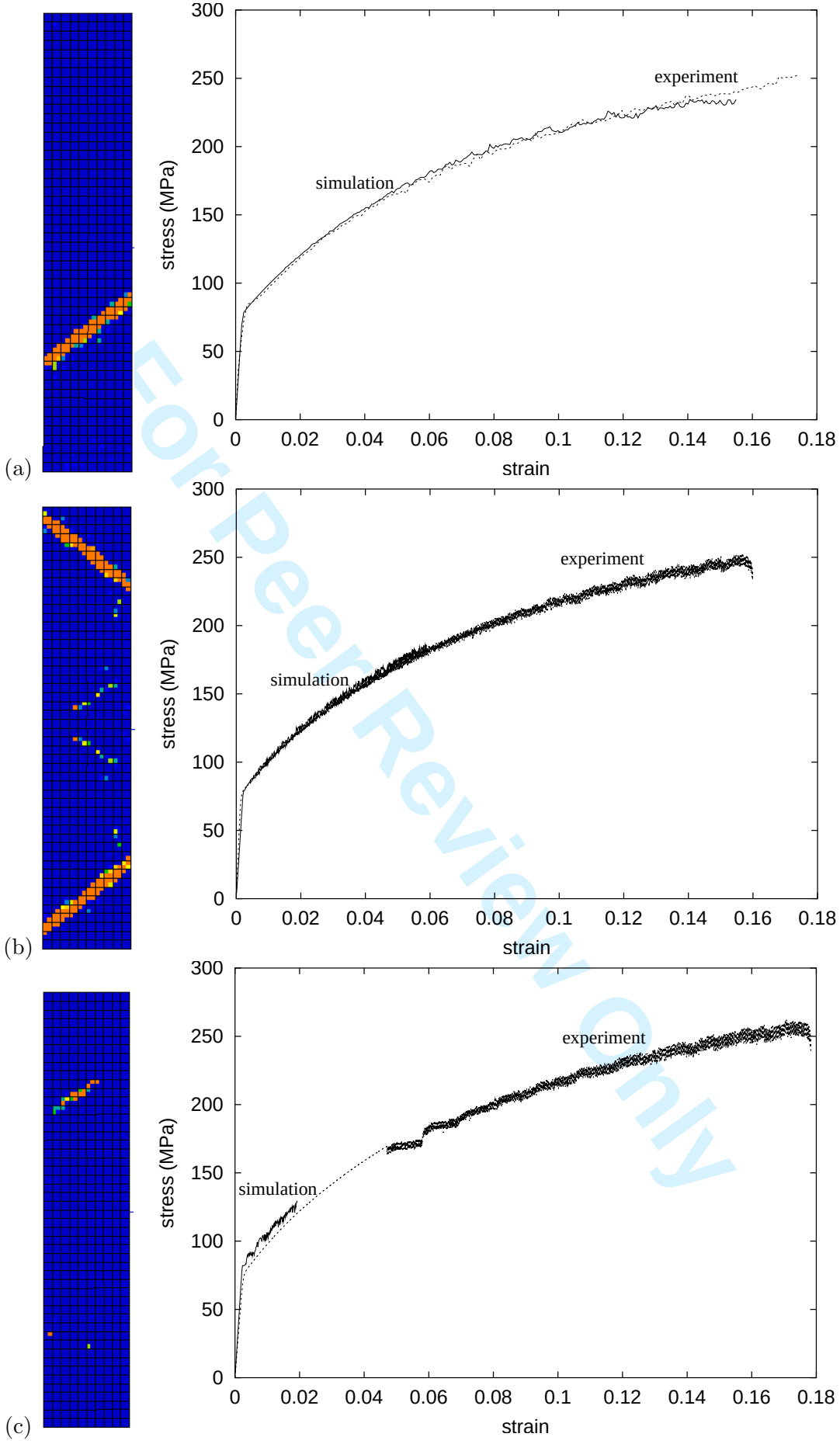

Figure 3. Comparison of the experimental and simulated stress–strain curves for the parent Al-3% Mg alloy at different applied strain rates: (a) $\dot{\varepsilon} = 6.2\ 10^{-3} s^{-1}$, (b) $\dot{\varepsilon} = 1.1\ 10^{-4} s^{-1}$, (c) $\dot{\varepsilon} = 1.1\ 10^{-5} s^{-1}$. The experimental curves are in dotted lines. For each strain rate, a typical distribution of the plastic strain rate $\dot{p}$ in the tensile plate is given. The red color corresponds to strain rates five times higher than the overall prescribed strain rate.

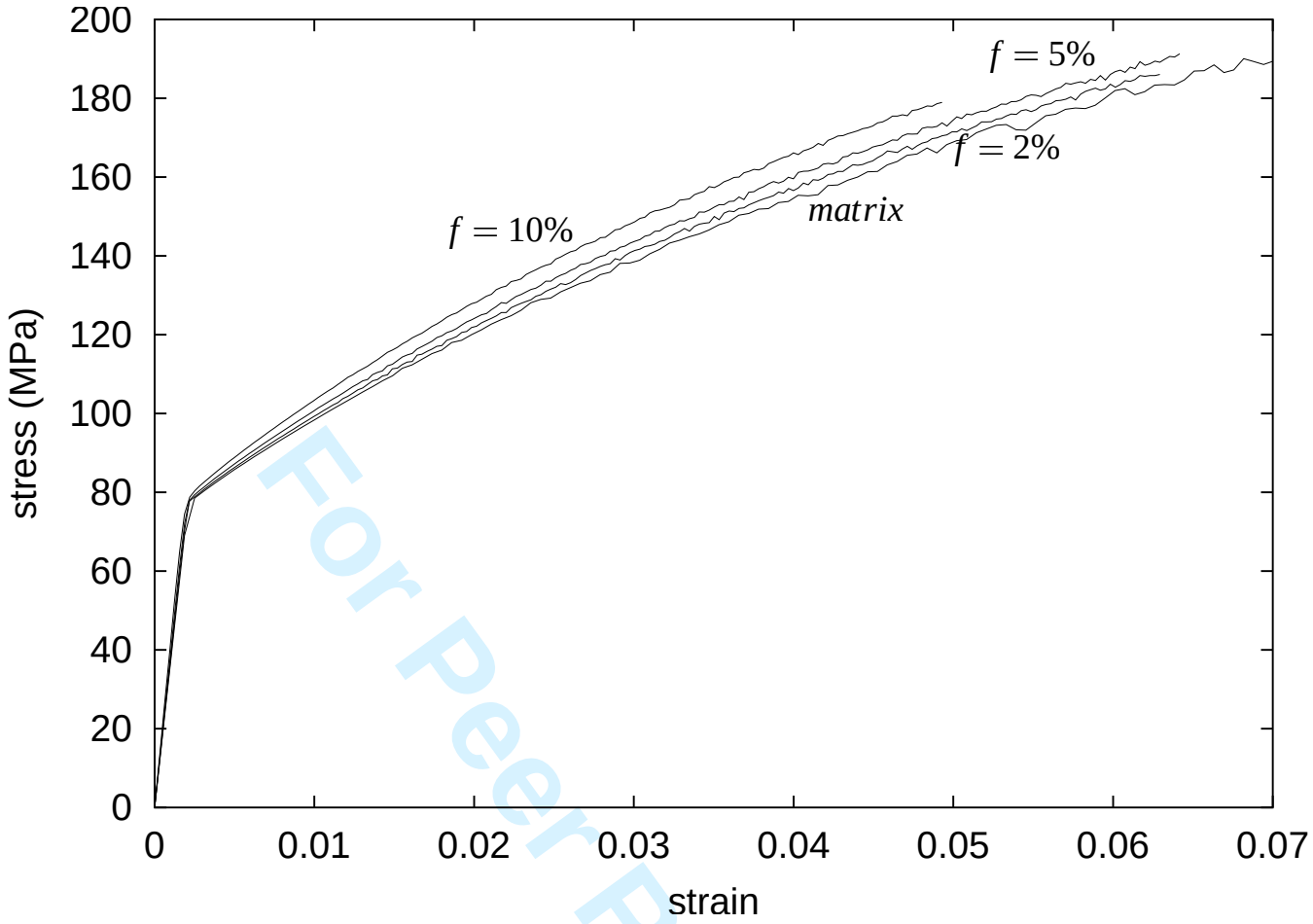

Figure 4. Influence of the volume fraction of particles on the computed stress–strain curves at $\dot{\varepsilon} = 6.2\ 10^{-3} s^{-1}$ for the AA5754 MMC. From the lower to the upper curves we have successively: the parent Al-3% Mg alloy, the AA5754 MMC with $f = 2\%$, the AA5754 MMC with $f = 5\%$, and the AA5754 MMC with $f = 10\%$.

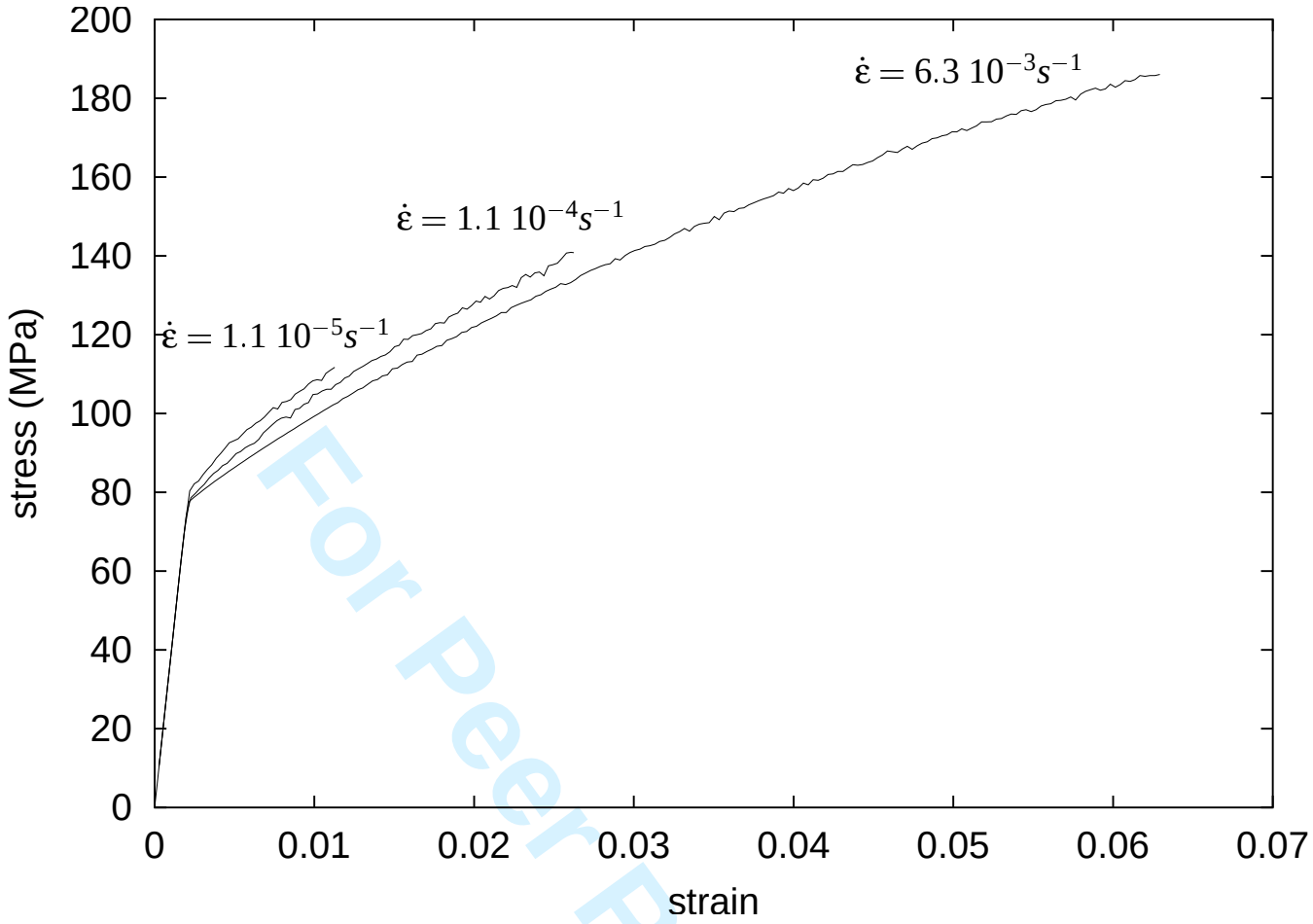

Figure 5. Influence of the applied strain rate on the computed stress–strain curves for the AA5754 MMC with $f = 2\%$.

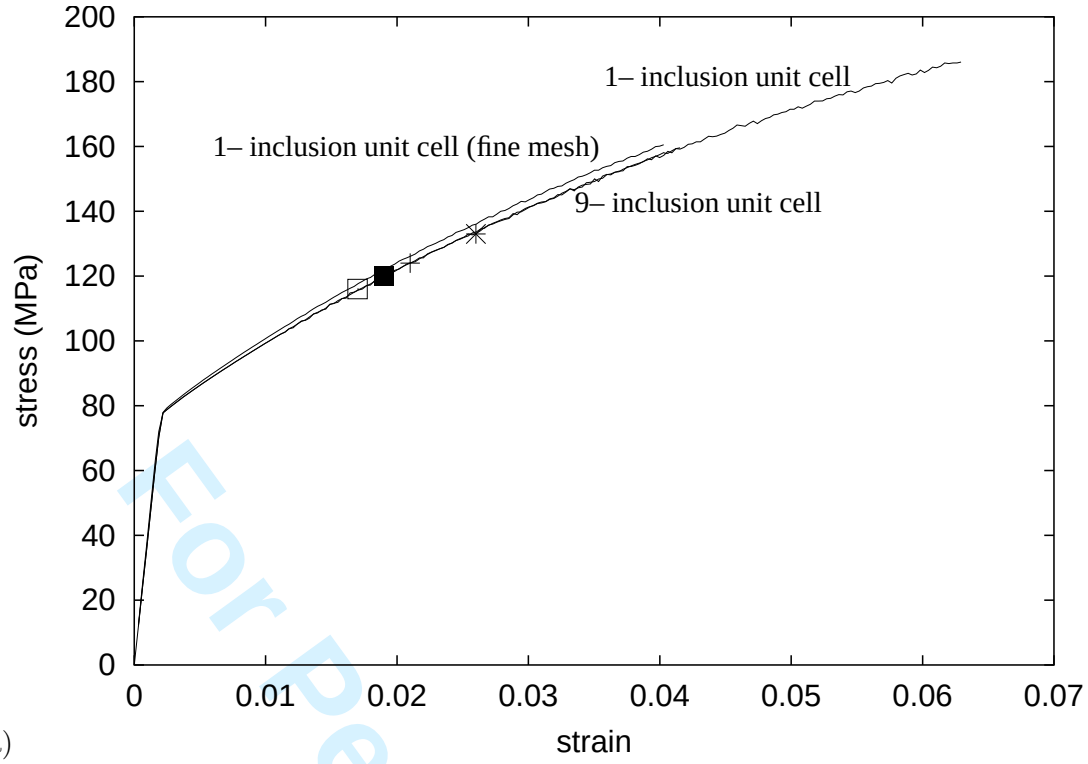

(a)

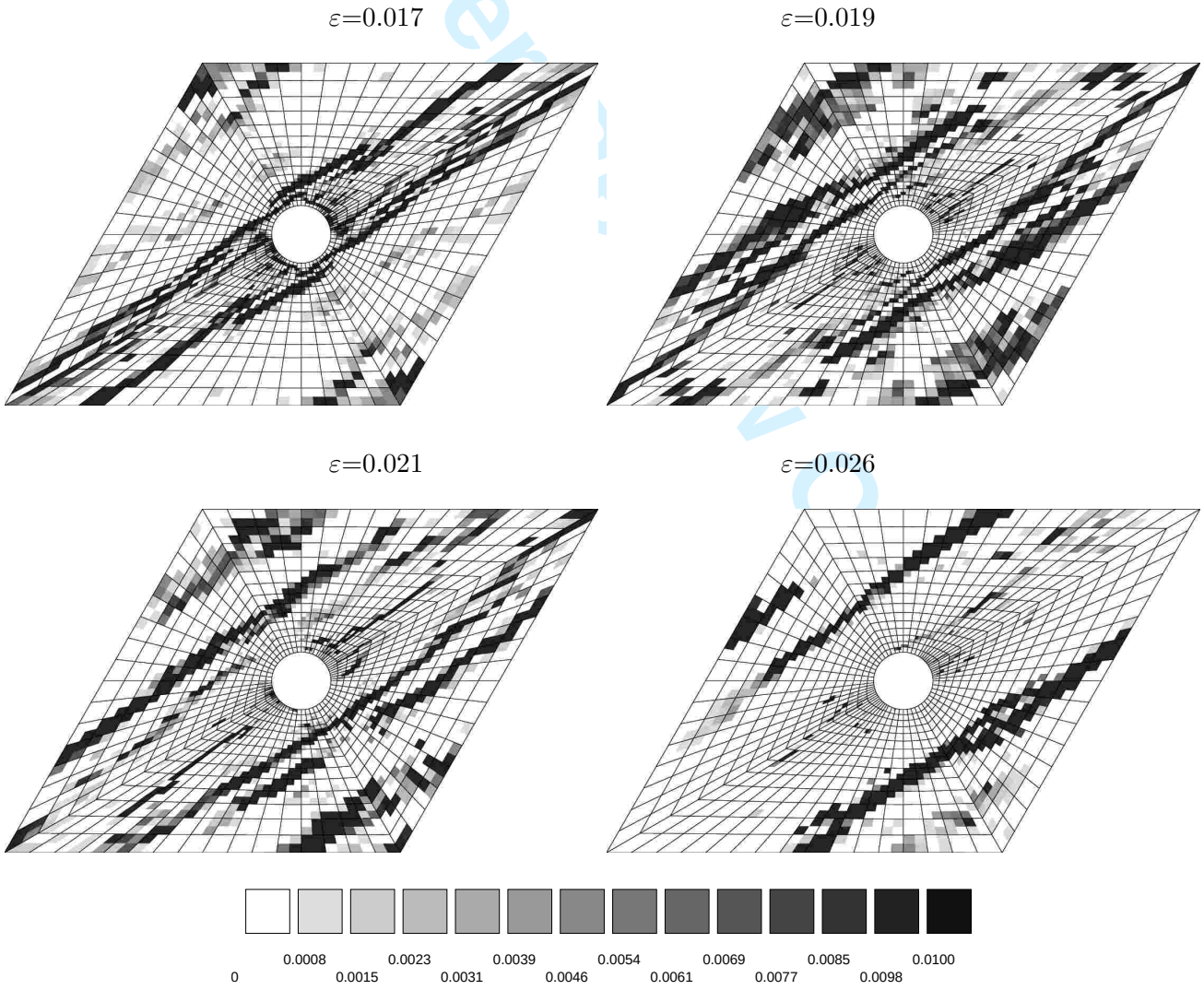

(b)

Figure 6. (a) Influence of mesh refinement and of the choice of the unit cell on the stress–strain curves for the AA5754 MMC with $f = 2\%$ at $\dot{\varepsilon} = 6.2\ 10^{-3} s^{-1}$; (b) maps of plastic strain rate (in s^{-1}) in the 1–inclusion cell ($f = 2\%$), at different mean strain levels which are indicated on the macroscopic curve (a).

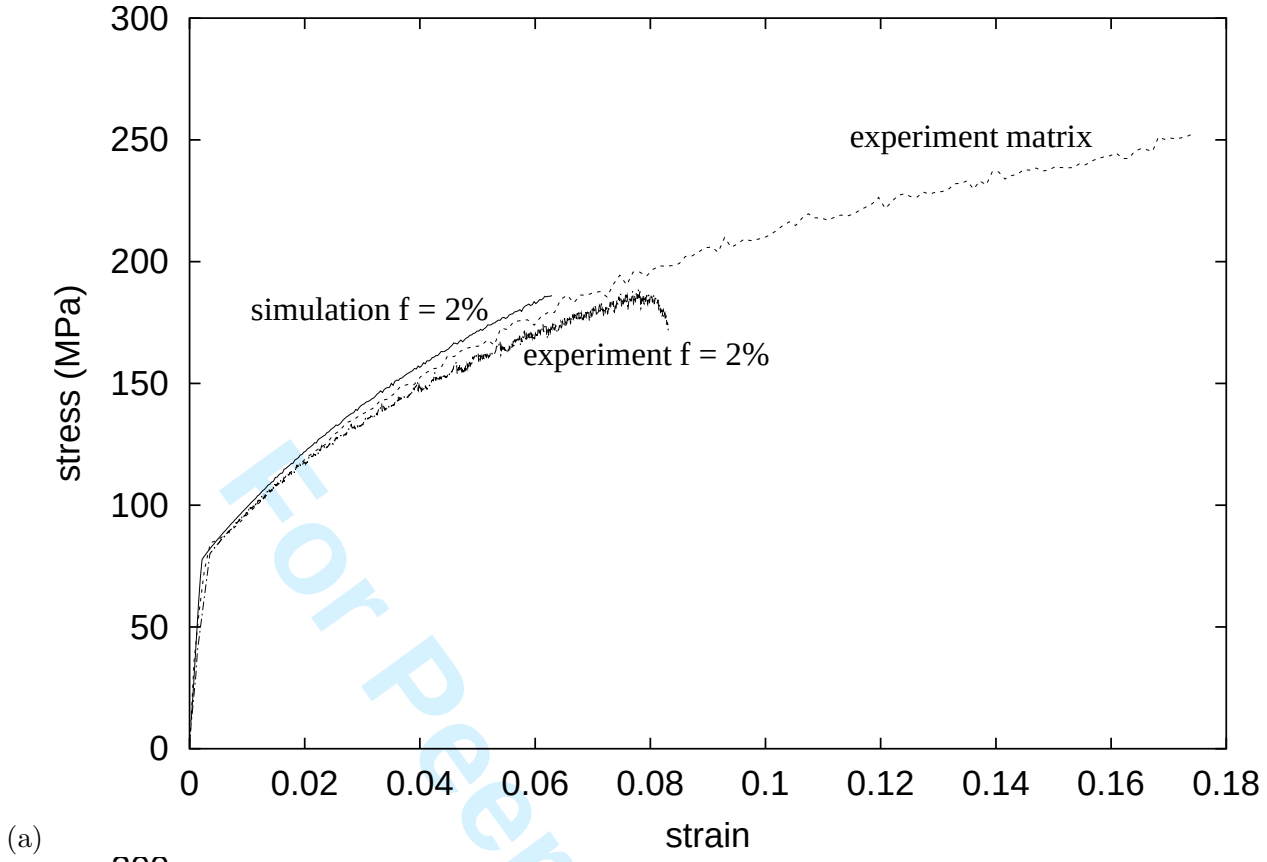

(a)

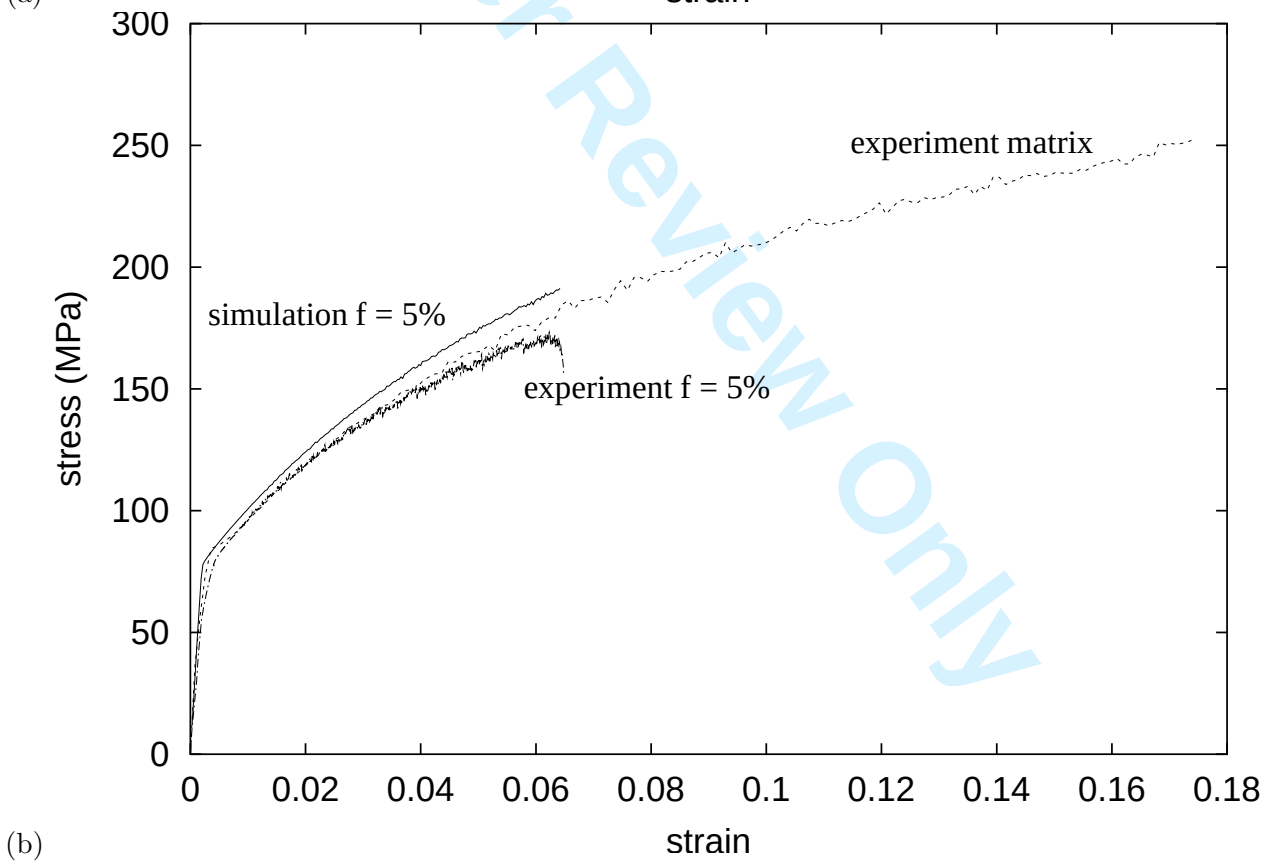

(b)

Figure 7. Comparison of the experimental and simulated stress–strain curves between the parent Al-3% Mg alloy and the AA5754 MMC at room temperature at $\dot{\varepsilon} = 6.2\ 10^{-3} s^{-1}$ with: (a) $f = 2\%$, (b) $f = 5\%$.

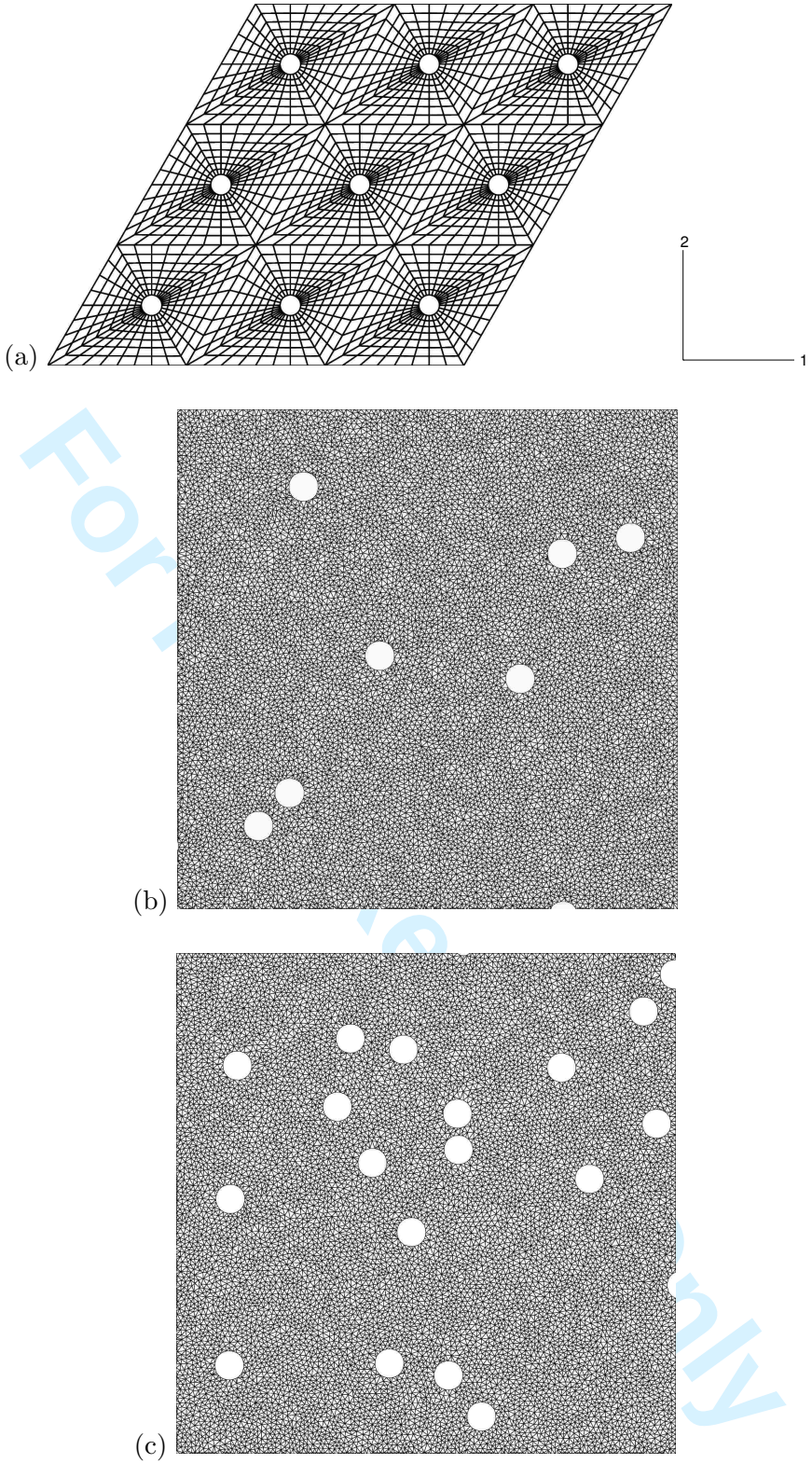

Figure 8. FE meshes for periodic and random distributions of particles: (a) periodic mesh with 9–inclusion unit cell with $f = 2\%$, (b) mesh with a random distribution of particles with $f = 2\%$, (c) mesh with a random distribution of particles with $f = 5\%$. The axes indicated in (a) are also valid for (b) and (c).

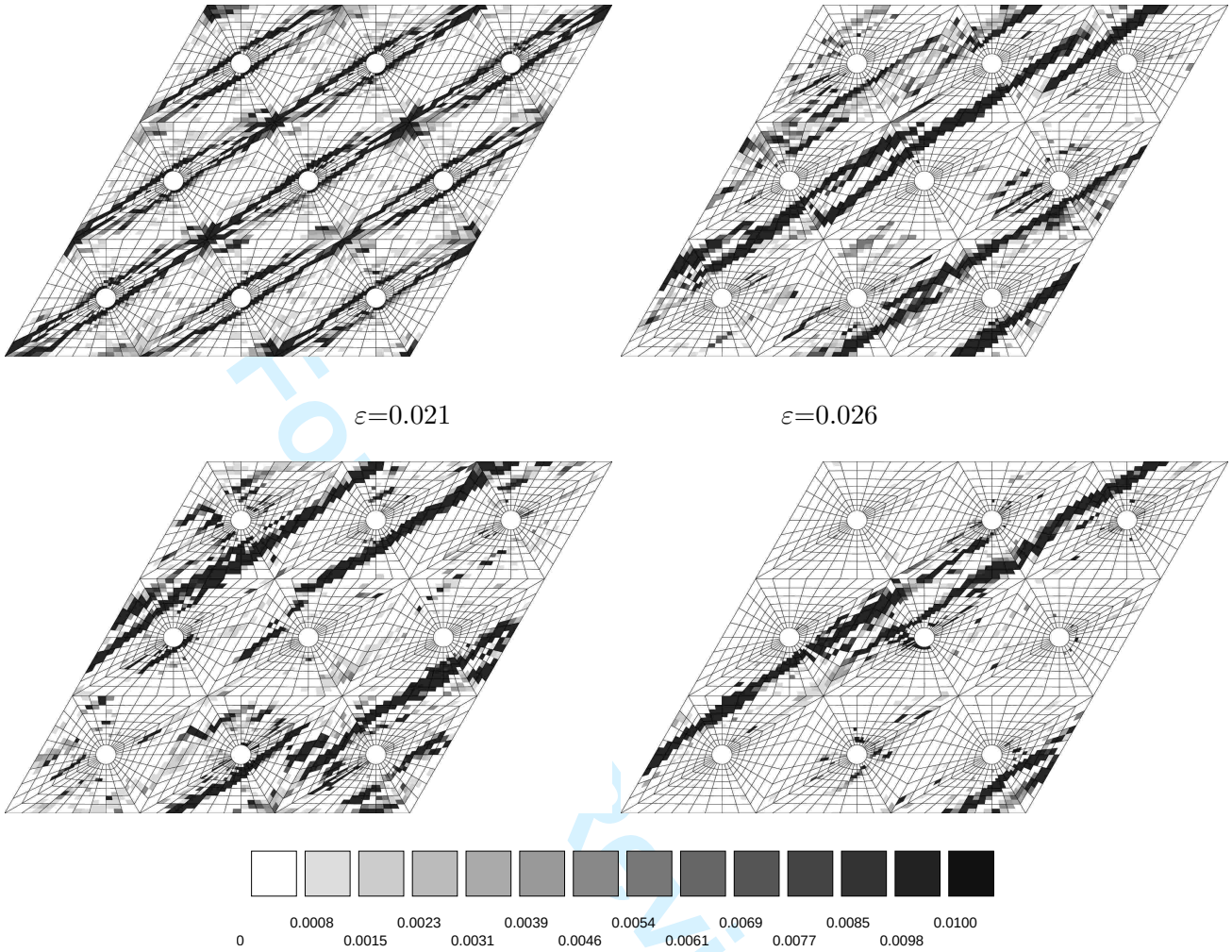

Figure 9. Maps of plastic strain rate (s^{-1}) in the 9–inclusion unit cell with the periodic distribution of particles for $f = 2\%$. at different mean strain levels indicated by symbols on the macroscopic curve of figure 6(a). The tensile axis is vertical.

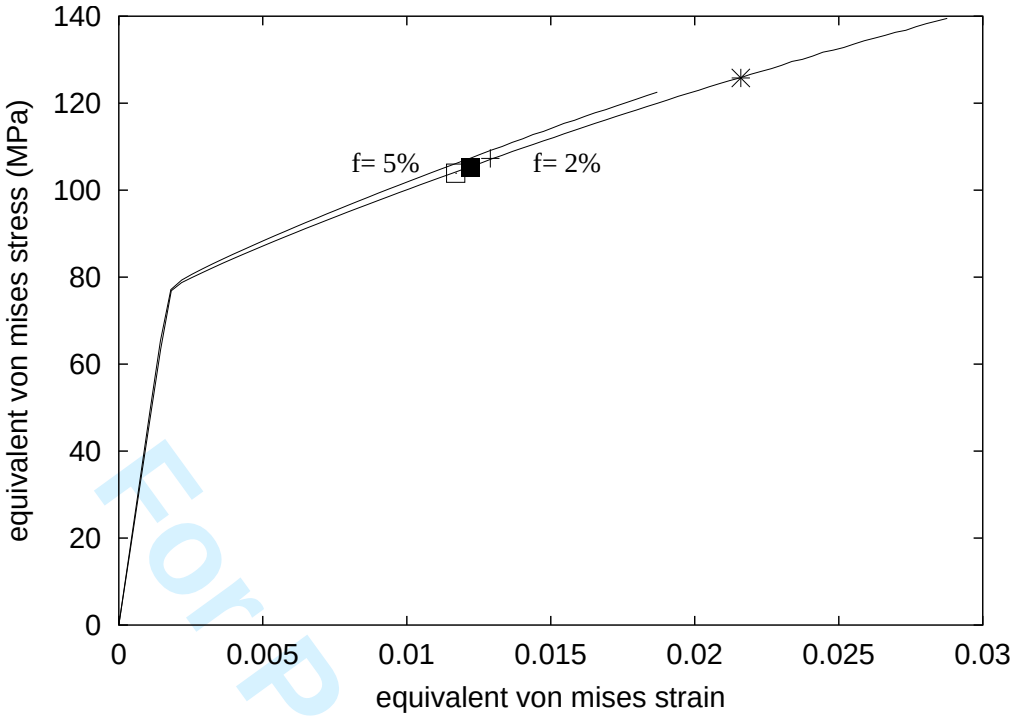

Figure 10. Influence of particle volume fraction f on the computed stress–strain curves for the AA5754 MMC in tension at $\dot{\varepsilon} = 6.2\ 10^{-3} s^{-1}$. Simulation with a random distribution of particles. The symbols indicate the strain levels corresponding to the plastic strain rate maps given in figure 11.

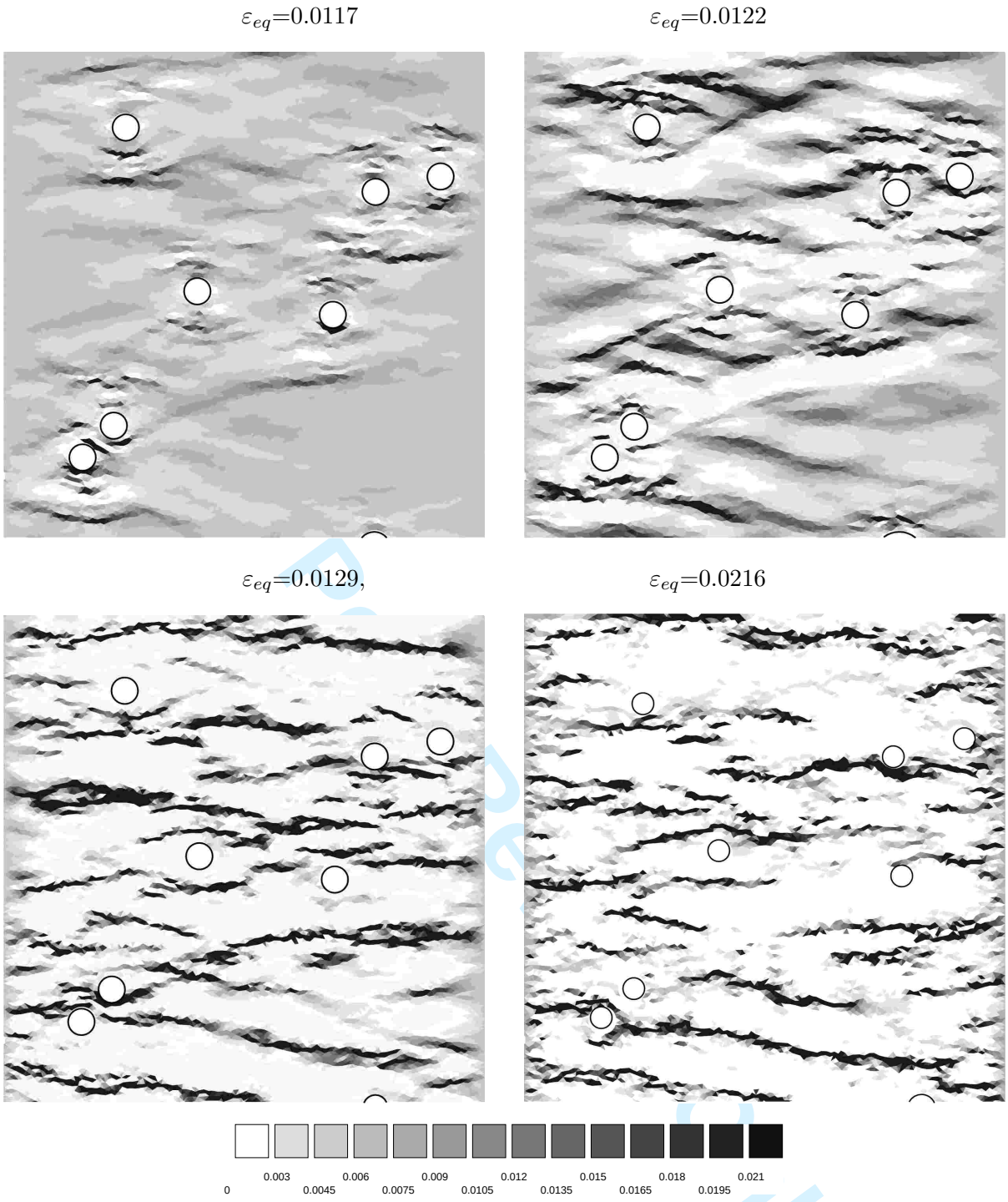

Figure 11. Maps of plastic strain rate (s^{-1}) in a random distribution of particles ($f = 2\%$) loaded in tension at different strain levels indicated by symbols on the macroscopic curve of figure 10. The tensile axis is vertical.

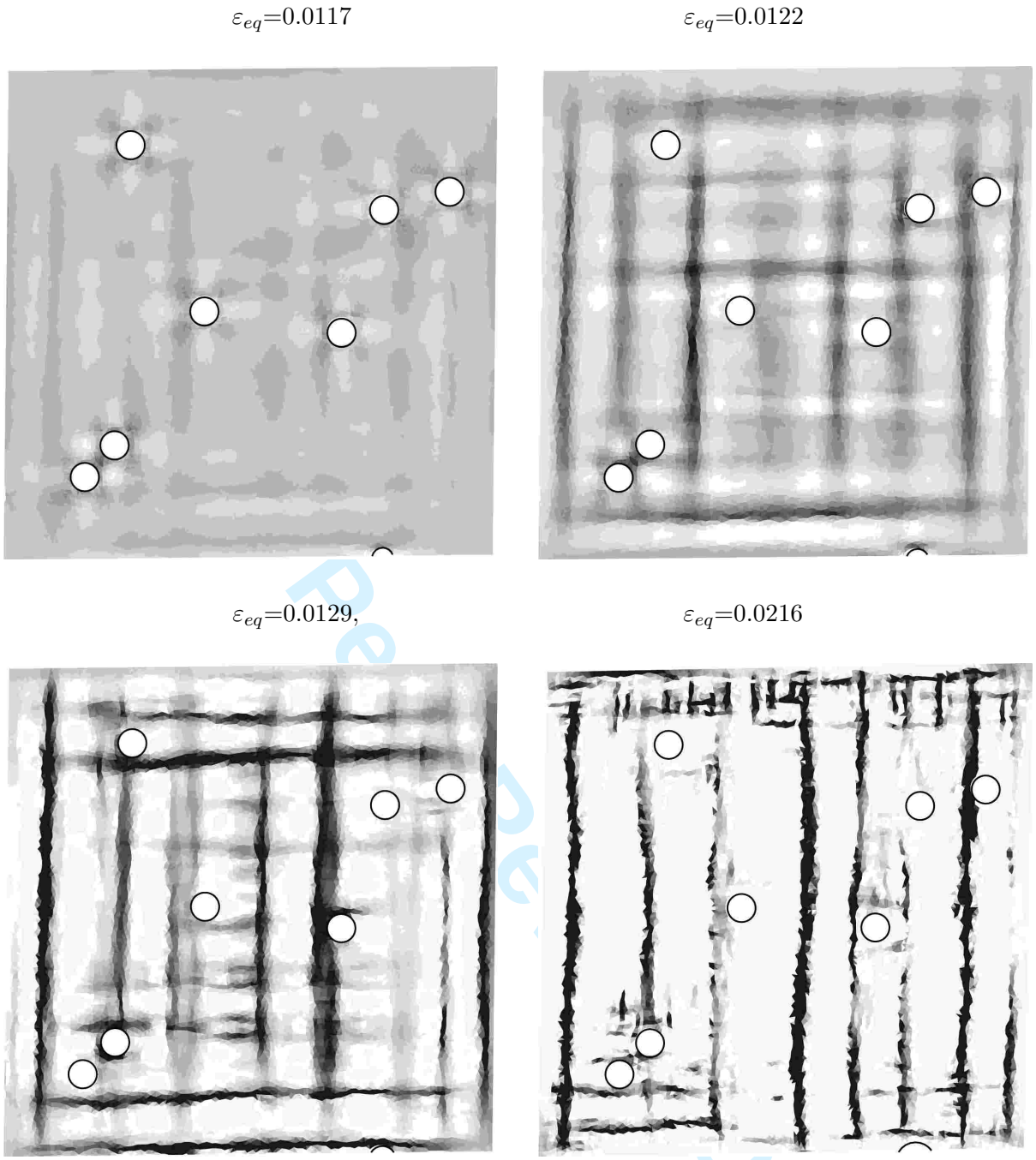

Figure 12. Maps of plastic strain rate (s^{-1}) in a random distribution of particles ($f = 2\%$) loaded in shear at different strain levels. The shearing axes are horizontal and vertical respectively.

ε_{eq}=0.0117

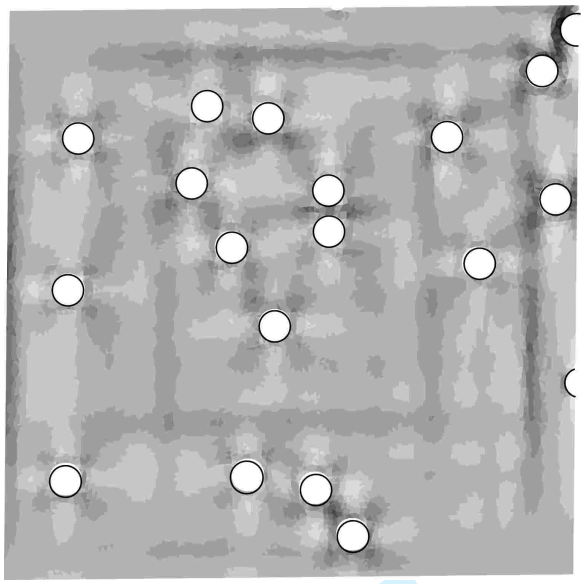

ε_{eq}=0.0122

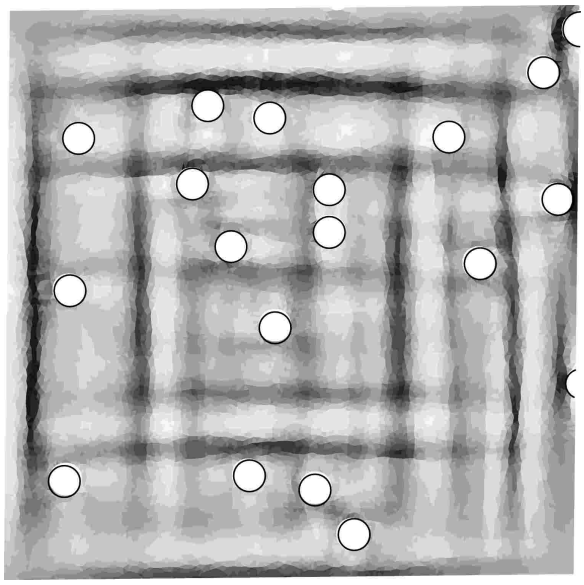

ε_{eq}=0.0129,

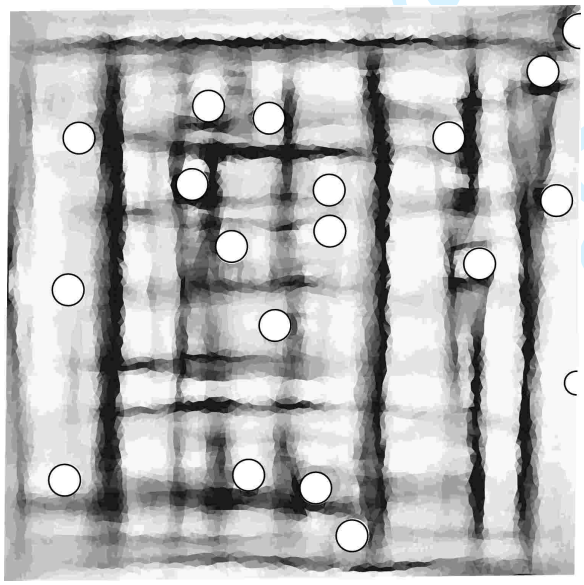

ε_{eq}=0.0216

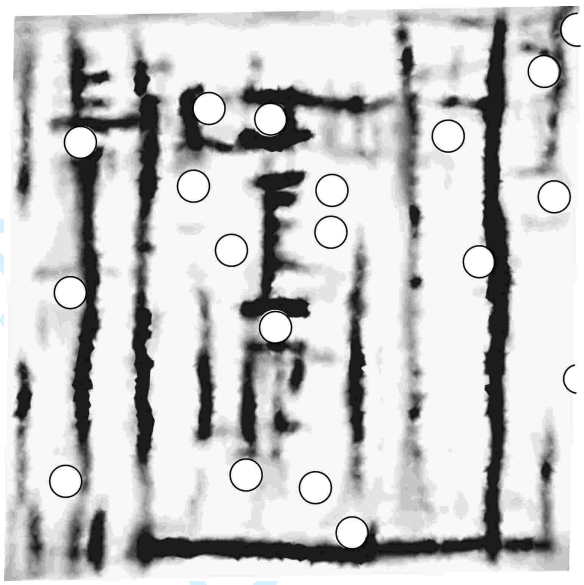

Figure 13. Maps of plastic strain rate (s^{-1}) in a random distribution of particles ($f = 5\%$) loaded in shear at different strain levels.

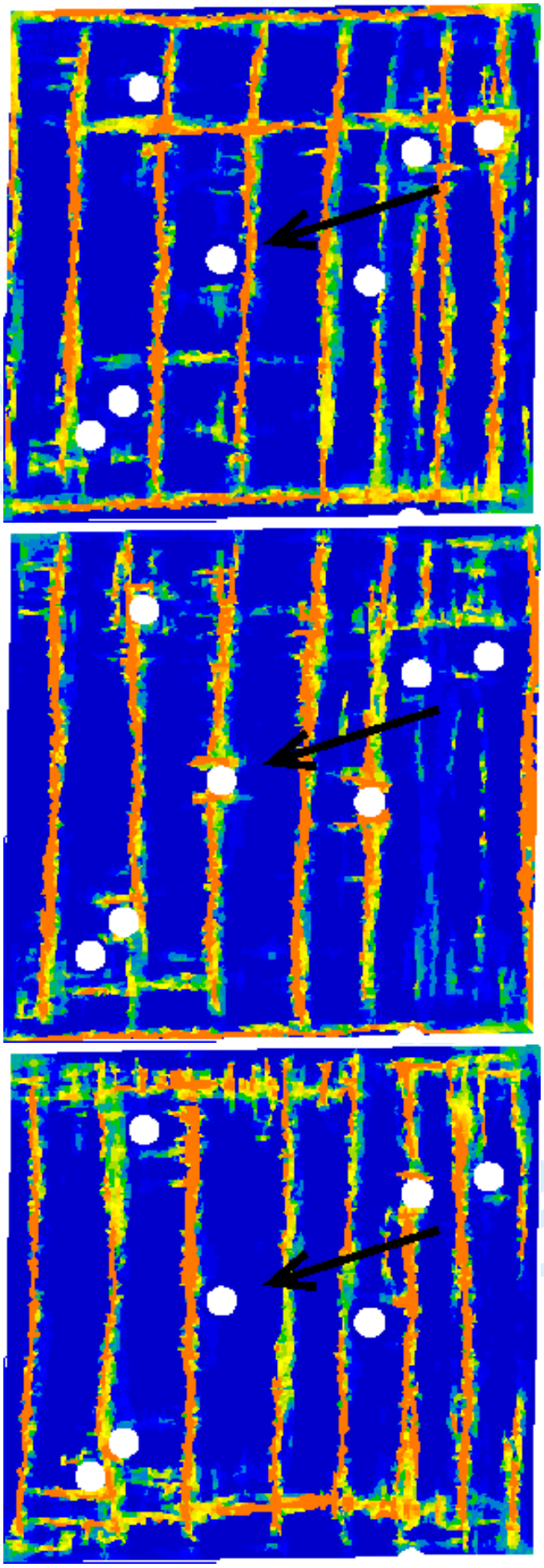

Figure 14. Overcoming of obstacles by the PLC band in a MMC with f =2% subjected to shear loading conditions. The arrow indicates the location of a particle for which the scattering of the band is clearly visible when it hits the obstacle.